Slip Control for a Three-Wheeled Electric Motorcycle

Andreas Karlin

LUND UNIVERSITY

Department of Automatic Control

MSc Thesis
TFRT-6128
ISSN 0280-5316

Department of Automatic Control
Lund University
Box 118
SE-221 00 LUND
Sweden

Printed in Sweden by Tryckeriet i E-huset
Lund 2021

Abstract

The aim of this Master Thesis was to design, implement and test a slip controller for an electric three-wheeled motorcycle in order to prevent undesirable slip on the driving wheel during acceleration and regenerative braking. A PI controller was implemented for the two different cases and was tested through various experiments and driving conditions. Three different control strategies were also designed and compared through simulations, a PI, LQR and a MPC controller for both acceleration and braking were designed and tested through five different driving conditions. All three controllers show promising results to control the slip and the implemented PI controller was also able increase safety on slippery surfaces.

Acknowledgements

I would first like to thank Ola Svensson and Omotion AB for giving me the opportunity to do an exciting thesis work, I have learned a lot during my time at Omotion AB. I wish Omotion AB all the best in the future. Secondly I would like to thank my supervisors from the Department of Automatic Control at LTH, Anders Robertson and Björn Olofsson, for all their guidance and feedback throughout this thesis. I am very grateful for that they have taken interest in my work, their time and the discussions we've had through our meetings. I could not have asked for better supervisors. I would also like to thank my examiner Rolf Johansson. Last but not least I would like to thank my partner Linn and my family for their endless support and their unconditional love over the years.

Contents

1

Introduction

1.1 Background

In the last decades advancements in computing power, actuators, sensors and control theory have led to vehicles that consist of many different control systems which assist the driver, increase safety and improve fuel consumption. Common systems in modern vehicles today are the electronic stability program (ESP), which prevents lateral instability of the vehicle and the anti-lock brake system (ABS) that prevents the wheels to lock-up during braking [Rajamani, 2012]. Slip control is also a common system. It controls the longitudinal slip dynamics of the wheels in order to obtain a desired slip value. These systems have been most common in vehicles with an internal combustion engine. Due to increased demands on the vehicle manufacturers to lower emissions and fuel consumption, the research interests have increased for hybrid and electric vehicles in both industry and the academic world [Eriksson and Nielsen, 2014]. This increased interest in electric vehicle technology has led to that these safety systems have also found their way to the electric vehicles, which has opened new doors in terms of different technologies compared to the more conventional vehicles. Today electric cars come with independent motors on each wheel, which enables controlling both the driving torque and the braking torque on each wheel independently. Hybrid and electric vehicles also enable use of regenerative braking with the means to recover some of the kinetic energy that goes into braking by letting the electric motors act as generators. This way the range of the vehicle can be extended since the battery is charged during regenerative braking. It also spares the conventional hydraulic brakes from wear and tear since they are not used to the same extent.

1.2 Motivation

Omotion AB is a start-up company that develops a three-wheeled electric motorcycle called Omotion ETR [Omotion, 2021a]. The company is currently developing a new version of the ETR that will bring some new improved features compared

to its predecessor. One of the new features that will be introduced is slip control, which prevents the rear wheel from slipping during hard accelerations or slippery surfaces. The slip controller should also prevent the rear wheel from locking up during regenerative braking.

1.3 Objective

The main objective of this Master Thesis is to design, implement and test a slip controller which prevents the rear wheel from slipping during hard acceleration or on low-friction surfaces for an electric three-wheeled motorcycle. The controller should also be able to prevent the rear wheel from locking up when regenerative braking is used. A study of three different control structures compared through simulations will also be carried out. The controller will be tested in experiments.
This thesis aims to answer the following questions:

- What type of controller is suitable for slip control on an electric three-wheeled motorcycle? How accurate model of the vehicle and its interaction with the road is needed in order to get a good performing slip control?
- Is it possible to use the same type of controller to prevent the rear wheel from locking up during regenerative braking? If not, what type of method can be used instead?
- Can the range of the electric three-wheeled vehicle be improved and will the acceleration of it be improved by incorporating slip control?
- Is it possible to improve the onboard measurement/ estimation of the longitudinal velocity by incorporating an accelerometer? How will it affect the slip control?

1.4 Related Research

A lot of research and developments in traction and slip control have been made. In the research community, a lot of work has been made in model predictive control by the authors of for example [Basrah et al., 2017], [Yuan et al., 2015], [Bonci et al., 2018]. Sliding mode control has also been used for slip control in research such as [Tanelli et al., 2009], [Amodeo et al., 2010] and [Hamzah et al., 2012]. In [Vasiljevic et al., 2012] a PI controller with an on-line road condition estimation for a three-wheeled electric car is investigated. In the work of [Johansen et al., 2003] a gain–scheduled LQR controller is proposed and investigated for slip control of a car. This thesis is based on research of [Basrah et al., 2017], [Vasiljevic et al., 2012] and [Johansen et al., 2003].

1.5 Contribution

This Master Thesis contributes with gained knowledge in vehicle dynamics of an electric three-wheeled motorcycle and control systems regarding it, but also simulations and experiments for validating performance.

2

Electric Vehicle

In this chapter we introduce the electric vehicle which the slip controller has been developed for, some technical data of the vehicle are presented and the available hardware and sensors are described.

2.1 Vehicle

The vehicle is an electric three-wheeled motorcycle developed by Omotion AB, called Omotion 2. It consists of two wheels at the front and one wheel at the rear. The electric motor is a so called hub motor mounted to the rear wheel, i.e., it is only the rear wheel that is the driving wheel. There is no gears in the motor, so the relation between the speed of the motor and the rear wheel is 1:1. In Table 2.1 some technical specifications of the vehicle can be found.

Table 2.1: Technical specifications of the Omotion 2.

Technical Specifications	
Vehicle mass:	350 kg
Max power:	24 kW
Continuous power:	11 kW
Max motor rpm:	1150
Battery voltage:	72 V
Battery capacity:	156 Ah, 11.2 kWh
Range:	140 km
Length:	2780 mm
Width:	1660 mm
Height:	1160 mm

2.2 Hardware & Sensors

The Electronic Control Unit (ECU) of the vehicle is developed by Omotion AB themselves and it consists of:

- 32-bit Arm processor
- Accelerometer
- Gyroscope

The vehicle is equipped with ABS brakes and the system comes with Hall sensors to measure the velocity of the front wheels which is used to estimate the velocity of the vehicle. The hub motor also comes with Hall sensors mounted on the inside of the motor and these are used to estimate the velocity of the rear wheel.

2.3 Anti-Lock Brake System

The purpose of modern anti-lock brake systems is to prevent the wheels from locking up and maximizing the braking force during hard braking. By preventing the wheels from locking, the braking distance will be reduced and control of the vehicle stability is retained [Bosch, 2011]. There are two common types of ABS methods used in industry, namely the deceleration-based algorithm and slip-based algorithms [Rajamani, 2012], [Kiencke and Nielsen, 2005].

2.4 Regenerative Braking

As mentioned in Section 1.1 the range of hybrid and electric vehicles can be extended by using regenerative braking [Rajamani, 2012], [Liang and Lin, 2010]. By letting the electric motors act as generators during the braking phase, the kinetic energy can be recovered which otherwise would be dissipated as frictional heat. This is done by inverting the current to the motors and letting the generated energy charge the battery. From a slip-control perspective this can be a challenge since the motors will apply an extra braking force in addition to the braking force from the hydraulic brakes, which might lead to locking up the wheels and thereby losing control of the vehicle. This can be prevented by controlling the wheel slip by letting the negative current act as reference for the controller and then consider the braking force from the hydraulic brakes as a disturbance, since the braking force is unknown in this case. This will ensure safety and maximize the recovered energy.

3

Modelling

In this chapter the equations for the longitudinal dynamics of the vehicle will be presented. A nonlinear and a linear state-space model will also be derived for simulation and control design.

3.1 Vehicle Dynamics

Consider a vehicle in motion along the road, assuming only longitudinal forces acting on the vehicle. The equation of motion along the longitudinal direction can then be written as [Rajamani, 2012]:

$$m\dot{V}_{\mathrm{x}} = F_{\mathrm{xf}} + F_{\mathrm{xr}} - F_{\mathrm{aer}} - R_{\mathrm{xf}} - R_{\mathrm{xr}} - F_{\mathrm{g}} \tag{3.1}$$

where m, V_{x} are the mass and the velocity of the vehicle respectively. $F_{\mathrm{xf}}, F_{\mathrm{xr}}$ are the longitudinal tire forces for the wheels at the front and the rear, respectively. F_{aer} is the aerodynamic drag force, $R_{\mathrm{xf}}, R_{\mathrm{xr}}$ are the rolling friction force acting on the front and the rear wheels. F_{g} is the gravitational force, $F_{\mathrm{g}} = mg\sin\theta$, where g is the gravity and $\sin\theta$ is the inclination of the road. Figure 3.1 shows how the forces are acting on the vehicle.

Tire Forces

A short introduction to the tire forces is presented here and the topic will be discussed in more detail later. The frictional tire forces F_{xi} due to the contact of the tires with the ground can be modeled in different ways. These forces are dependent on the normal load on each tire, the friction coefficient of the interface between the tire and the road and the slip ratio [Rajamani, 2012].

Slip ratio The longitudinal slip is defined as the difference between the velocity of the vehicle and the linear velocity of the wheels $V_{\mathrm{x}} - r_{\mathrm{eff}}\omega$, where r_{eff} and ω is the effective radius of the wheel and the angular velocity of the wheel, respectively. The slip ratio is defined as [Rajamani, 2012]:

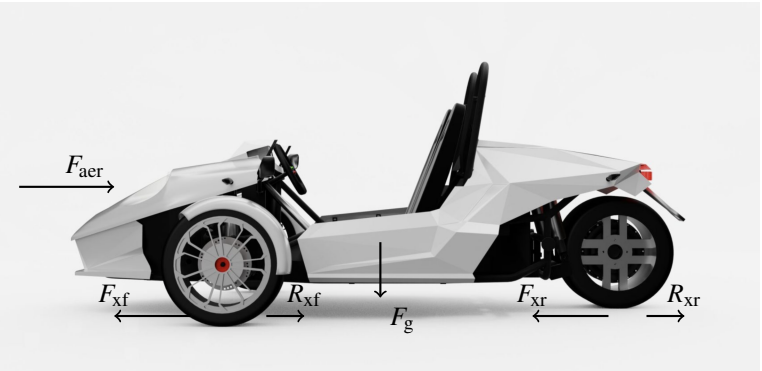

Figure 3.1: Longitudinal forces acting on the vehicle. Figure from [Omotion, 2021b]

.

$$\lambda_a = \frac{r_{eff}\omega - V_x}{r_{eff}\omega} \tag{3.2}$$

$$\lambda_b = \frac{r_{eff}\omega - V_x}{V_x} \tag{3.3}$$

where λ_a and λ_b are the slip ratio under acceleration and under braking, respectively. In Figure 3.2 typical slip curves for different road conditions can be seen. The parameters for the slip curves in Figure 3.2 can be found at [Mathworks, 2021].

Aerodynamic Drag Force

The aerodynamic drag force acting on the vehicle can be written as [Rajamani, 2012]:

$$F_{aer} = \frac{1}{2}\rho C_d A_f (V_x + V_{wnd})^2 \tag{3.4}$$

where ρ is the mass density of air, C_d is the coefficient of the aerodynamic drag, V_{wnd} is the velocity of the wind and A_f is the area of the front of the vehicle.

Rolling Frictional Force

The rolling frictional force can be approximated as [Rajamani, 2012]:

$$R_x = \mu_f F_z \tag{3.5}$$

where μ_f is the rolling friction coefficient and F_z is the normal force on the tire.

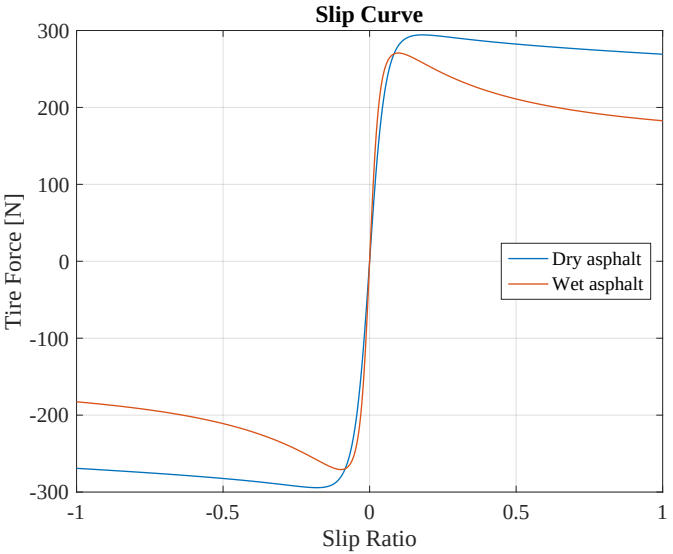

Figure 3.2: Slip curves for different road conditions on asphalt.

Normal Force

The normal force on the wheels is dependent on the total weight of the vehicle, the location of the center of gravity, the acceleration of the vehicle, the aerodynamic drag forces and the inclination of the road [Rajamani, 2012]. The normal forces on the front and the rear tires can be described respectively as:

$$F_{\mathrm{zf}} = \frac{-F_{\mathrm{aer}} h_{\mathrm{aer}} - mh\dot{V}_{\mathrm{x}} - mgh\sin\theta + mgl_{\mathrm{r}}\cos\theta}{l_{\mathrm{f}} + l_{\mathrm{r}}} \tag{3.6}$$

$$F_{\mathrm{zr}} = \frac{F_{\mathrm{aer}} h_{\mathrm{aer}} + mh\dot{V}_{\mathrm{x}} + mgh\sin\theta + mgl_{\mathrm{f}}\cos\theta}{l_{\mathrm{f}} + l_{\mathrm{r}}} \tag{3.7}$$

where h_{aer} is the height of the location at which the aerodynamic force acts, m is the mass of the vehicle, h is the height of the center of gravity, g is the gravity and l_{f}, l_{r} is the longitudinal distance of the front- and rear axle from the center of gravity of the vehicle.

3.2 Wheel Dynamics

The dynamics of the wheels are given by:

$$J_{\mathrm{w}}\dot{\omega}_{\mathrm{i}} = T_{\mathrm{m}} - T_{\mathrm{b}} - r_{\mathrm{eff}} F_{\mathrm{xi}} \ , \mathrm{i} = \mathrm{f}, \mathrm{r} \tag{3.8}$$

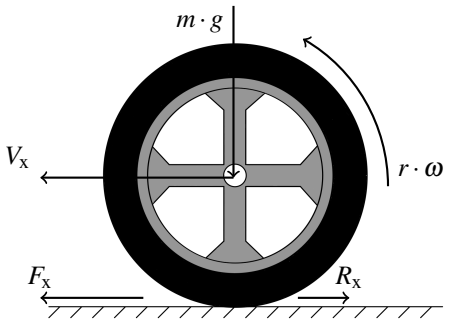

Figure 3.3: Wheel dynamics.

where J_w is the moment of inertia of the wheel, $\dot{\omega}$ is the angular acceleration of the wheel, T_m is the applied torque from the motor and T_b is the applied torque from the brakes [Rajamani, 2012]. Figure 3.3 illustrates the dynamics of the wheel.

3.3 Tire Dynamics

Small Slip Ratio

For small slip ratios the longitudinal tire forces can be modeled as being proportional to the slip ratio [Rajamani, 2012]:

$$F_x = C_\lambda \lambda \tag{3.9}$$

where C_λ is the longitudinal tire stiffness parameter. However for larger slip ratios, the linear model in (3.9) is not feasible anymore and a nonlinear model is needed to describe the dynamics. One such model is the Magic Formula which is described next.

The Magic Formula Tire Model

The Magic Formula developed by Pacejka and Bakker can be used to model the slip ratio of both the longitudinal and the lateral tire forces and the alignment moment [Rajamani, 2012]. The expression and its coefficients is based on empirical experiments. In the case where only the longitudinal force is considered, the tire force F_x is given in [Rajamani, 2012]:

$$F_x = D \sin\left[C \arctan(BX - E(BX - \arctan(BX)))\right] + S_v \tag{3.10}$$

where $X = \lambda - S_h$ and

B: stiffness factor
C: shape factor
D: peak value
E: curvature factor
S_h: horizontal shift
S_v: vertical shift

Dugoff's Tire Model

An alternative to the Magic Formula is Dugoff's tire model [Rajamani, 2012], which compared to the Magic Formula is derived analytically. The longitudinal tire force is given by:

$$F_x = C_\lambda \frac{\lambda}{1+\lambda} f(\sigma) \tag{3.11}$$

where

$$\sigma = \frac{\mu F_z (1+\lambda)}{2((C_\lambda \lambda)^2 + (C_\alpha \tan(\alpha))^2)^{1/2}} \tag{3.12}$$

and $f(\sigma) = (2-\sigma)\sigma$ if $\sigma < 1$ and $f(\sigma) = 1$ if $\sigma \geq 1$, where α is the lateral slip which is assumed zero in this case.

Burckhardt Approach

If the friction coefficient μ is not considered to be equal to 1, the tire forces can be modeled as [Savaresi and Tanelli, 2010]:

$$F_x = \mu(\lambda) F_z \tag{3.13}$$

where

$$\mu(\lambda) = a(1 - e^{-b\lambda}) - c\lambda \tag{3.14}$$

where a, b, c are parameters that determines the shape of the slip curve.

3.4 Single-corner Model

A common model for design of slip-control algorithms is the single-corner model. It is very simple, yet effective, where only one wheel is modelled. It is defined as [Savaresi and Tanelli, 2010]:

$$\dot{V}_x = \frac{1}{m} F_{xr} \tag{3.15}$$

$$\dot{\omega} = \frac{1}{J_w}(T_m - T_b - r_{eff} F_{xr}) \tag{3.16}$$

In this model, the dynamic load transfer due to the pitch motion is neglected. The normal force can then be modelled as $F_z = mg$.

The dynamics of the suspension system is also neglected and only straight-line acceleration and deceleration are considered whereas friction forces due to camber angle and side slip are neglected. The model is further simplified by ignoring the rolling resistance and the aerodynamic drag force.

3.5 Double-corner Model

In the double-corner model, one wheel at the front and one wheel at the rear are modelled. This way it is possible to incorporate the load transfer dynamics into the model. The dynamics of the vehicle is described by [Savaresi and Tanelli, 2010]:

$$\dot{V}_x = \frac{1}{m}F_{xf} + \frac{1}{m}F_{xr} \tag{3.17}$$

$$\dot{\omega}_f = \frac{1}{J_w}(-T_b - r_{eff}F_{xr}) \tag{3.18}$$

$$\dot{\omega}_r = \frac{1}{J_w}(T_m - T_b - r_{eff}F_{xr}) \tag{3.19}$$

where the normal force is defined by (3.6) and (3.7) for the front and the rear wheels, respectively.

3.6 State-Space Model

For control design, the single-corner model was used, where only the rear wheel is considered since the vehicle is rear–wheel driven. It is assumed that no slip occurs at the front wheels. Pacejka's tire model was used to describe the tire forces. The dynamics of the slip is derived by taking the derivative of the Equations (3.2) and (3.3):

$$\dot{\lambda}_a = \frac{V_x}{r\omega^2}\dot{\omega} - \frac{1}{r\omega}\dot{V}_x \tag{3.20}$$

$$\dot{\lambda}_b = \frac{r}{V_x}\dot{\omega} - \frac{r\omega}{V_x^2}\dot{V}_x \tag{3.21}$$

By inserting (3.15) and (3.16) in (3.20) and (3.21) the following equations are obtained:

$$\dot{\lambda}_a = -\frac{1}{V_x}\left(\frac{(1-\lambda)^2}{J_w}r^2 + \frac{1-\lambda}{m}\right)F_x + \frac{(1-\lambda)^2}{J_w V_x}(T_m - T_b) \tag{3.22}$$

and

$$\dot{\lambda}_b = -\frac{1}{V_x}\left(\frac{1+\lambda}{m} + \frac{r^2}{J_w}\right)F_x + \frac{r}{J_w V_x}(T_m - T_b) \tag{3.23}$$

Nonlinear State-Space Model

From (3.15), (3.22) and (3.23) a nonlinear state-space model based on V_x and λ_i is obtained for the dynamics of acceleration and braking, respectively:

Acceleration

$$\dot{V}_x = \frac{1}{m} F_{xr} \tag{3.24}$$

$$\dot{\lambda}_a = -\frac{1}{V_x}\left(\frac{1-\lambda}{m} + r^2\frac{(1-\lambda)^2}{J_w}\right)F_x + \frac{r(1-\lambda)^2}{J_w V_x}(T_m - T_b) \tag{3.25}$$

Braking

$$\dot{V}_x = \frac{1}{m} F_{xr} \tag{3.26}$$

$$\dot{\lambda}_b = -\frac{1}{V_x}\left(\frac{1+\lambda}{m} + \frac{r^2}{J_w}\right)F_x + \frac{r}{J_w V_x}(T_m - T_b) \tag{3.27}$$

Linearization

The nonlinear systems (3.24), (3.25), (3.26) and (3.27) can be written more compactly as:

$$\dot{\boldsymbol{x}}_i = \boldsymbol{f}(\boldsymbol{x}_i, \boldsymbol{u}_i) \tag{3.28}$$

where $\boldsymbol{x}_i$ and $\boldsymbol{u}_i$ represent the system states and inputs, respectively. The linearized system can be obtained by performing a Taylor expansion of the nonlinear system:

$$\dot{\boldsymbol{x}} = \dot{\boldsymbol{x}}(\boldsymbol{x}_0, \boldsymbol{u}_0) + \frac{\partial \boldsymbol{f}(\boldsymbol{x}_0, \boldsymbol{u}_0)}{\partial \boldsymbol{x}}(\boldsymbol{x} - \boldsymbol{x}_0) + \frac{\partial \boldsymbol{f}(\boldsymbol{x}_0, \boldsymbol{u}_0)}{\partial \boldsymbol{u}}(\boldsymbol{u} - \boldsymbol{u}_0) + \boldsymbol{h.o.t} \tag{3.29}$$

where $\boldsymbol{x}_0$ and $\boldsymbol{u}_0$ are the equilibrium points of the system. Then the linearized system can be written on the form:

$$\Delta\dot{\boldsymbol{x}} = \boldsymbol{A}\Delta\boldsymbol{x} + \boldsymbol{B}\Delta\boldsymbol{u} \tag{3.30}$$

where

$$\boldsymbol{A} = \frac{\partial \boldsymbol{f}}{\partial \boldsymbol{x}}(\boldsymbol{x}_0, \boldsymbol{u}_0) \tag{3.31}$$

$$\boldsymbol{B} = \frac{\partial \boldsymbol{f}}{\partial \boldsymbol{u}}(\boldsymbol{x}_0, \boldsymbol{u}_0) \tag{3.32}$$

The dynamics of the vehicle's velocity is much slower compared to the dynamics of the slip, and therefore the velocity can be considered as a slowly time-varying parameter. Thus the system can be reduced to a first-order model only considering the dynamics of the slip [Johansen et al., 2003].

The system is therefore only described by the slip dynamics equations:

$$\dot{\lambda}_{\mathrm{a}} = -\frac{1}{V_{\mathrm{x}}}\left(\frac{1-\lambda}{m} + r^2\frac{(1-\lambda)^2}{J_{\mathrm{w}}}\right)F_{\mathrm{x}} + \frac{r(1-\lambda)^2}{J_{\mathrm{w}}V_{\mathrm{x}}}(T_{\mathrm{m}} - T_{\mathrm{b}}) \tag{3.33}$$

$$= -\frac{1-\lambda}{V_{\mathrm{x}}}\left[\left(\frac{1}{m} + r^2\frac{1-\lambda}{J_{\mathrm{w}}}\right)F_{\mathrm{x}} + r\frac{1-\lambda}{J_{\mathrm{w}}}(T_{\mathrm{m}} - T_{\mathrm{b}})\right] \tag{3.34}$$

$$= -\frac{1-\lambda}{V_{\mathrm{x}}}\left[\alpha_{\mathrm{a}}F_{\mathrm{x}} - \beta_{\mathrm{a}}(T_{\mathrm{m}} - T_{\mathrm{b}})\right] \tag{3.35}$$

where

$$\alpha_{\mathrm{a}} = \frac{1}{m} + r^2\frac{1-\lambda}{J_{\mathrm{w}}} \tag{3.36}$$

$$\beta_{\mathrm{a}} = r\frac{1-\lambda}{J_{\mathrm{w}}} \tag{3.37}$$

and

$$\dot{\lambda}_{\mathrm{b}} = -\frac{1}{V_{\mathrm{x}}}\left(\frac{1+\lambda}{m} + \frac{r^2}{J_{\mathrm{w}}}\right)F_{\mathrm{x}} + \frac{r}{J_{\mathrm{w}}V_{\mathrm{x}}}(T_{\mathrm{m}} - T_{\mathrm{b}}) \tag{3.38}$$

$$= -\frac{1}{V_{\mathrm{x}}}\left[\alpha_{\mathrm{b}}F_{\mathrm{x}} - \beta_{\mathrm{b}}(T_{\mathrm{m}} - T_{\mathrm{b}})\right] \tag{3.39}$$

where

$$\alpha_{\mathrm{b}} = \frac{1+\lambda}{m} + \frac{r^2}{J_{\mathrm{w}}} \tag{3.40}$$

$$\beta_{\mathrm{b}} = \frac{r}{J_{\mathrm{w}}V_{\mathrm{x}}} \tag{3.41}$$

In order to obtain a linearized model of the system, one must first find the equilibrium points, λ_0 of the system, i.e., when $\dot{\lambda}_{\mathrm{i}} = 0$, we simply solve for λ_{i}^* that makes

$$\alpha_{\mathrm{i}}F_{\mathrm{x}} = \beta_{\mathrm{i}}(T_{\mathrm{m}} - T_{\mathrm{b}}) \tag{3.42}$$

The linearized dynamics during acceleration is given by:

$$\begin{aligned}\dot{\lambda}_{\mathrm{a}} &= -\frac{1}{V_{\mathrm{x}}}\left(-\frac{1}{m} - \frac{r^2}{J}2(1-\lambda_0)\right)F_{\mathrm{x}}\Delta\lambda \\ &- \left[\frac{1}{V_{\mathrm{x}}}\left(\frac{1-\lambda_0}{m} + \frac{r^2}{J}(1-\lambda_0)^2\right)\frac{\partial F_{\mathrm{x}}}{\partial\lambda}(\lambda_0) + \frac{2r}{J_{\mathrm{w}}V_{\mathrm{x}}}(1-\lambda_0)T_{\mathrm{m}_0}\right]\Delta\lambda \\ &+ r\frac{(1-\lambda_0)^2}{J_{\mathrm{w}}V_{\mathrm{x}}}\Delta T_{\mathrm{m}}\end{aligned}$$

and the linearized dynamics during braking is given by:

$$\dot{\lambda}_{\mathrm{b}} = -\frac{1}{V_{\mathrm{x}}}\left[\left(\frac{1+\lambda_0}{m}+\frac{r^2}{J_{\mathrm{w}}}\right)\frac{\partial F_{\mathrm{x}}}{\partial \lambda}(\lambda_0)+\frac{F_{\mathrm{x}}}{m}(\lambda_0)\right]\Delta\lambda+\frac{r}{J_{\mathrm{w}}V_{\mathrm{x}}}\Delta T_{\mathrm{m}}$$

Linear State-Space Model

To summarize the linear models for acceleration and braking they are given by the equation:

$$\dot{\boldsymbol{x}} = \boldsymbol{A}_{\mathrm{i}}\boldsymbol{x}+\boldsymbol{B}_{\mathrm{i}}\boldsymbol{u} \tag{3.43}$$

Acceleration

$$\begin{aligned}\boldsymbol{A}_{\mathrm{a}} = &-\frac{1}{V_{\mathrm{x}}}\left(-\frac{1}{m}-\frac{r^2}{J}2(1-\lambda_0)\right)F_{\mathrm{x}}(\lambda_0)\\ &-\frac{1}{V_{\mathrm{x}}}\left(\frac{1-\lambda_0}{m}+\frac{r^2}{J}(1-\lambda_0)^2\right)\frac{\partial F_{\mathrm{x}}}{\partial \lambda}(\lambda_0)\end{aligned} \tag{3.44}$$

and

$$\boldsymbol{B}_{\mathrm{a}} = \frac{r(1-\lambda_0)^2}{J_{\mathrm{w}}V_{\mathrm{x}}} \tag{3.45}$$

Braking

$$\boldsymbol{A}_{\mathrm{b}} = -\frac{1}{V_{\mathrm{x}}}\left[\left(\frac{1+\lambda_0}{m}+\frac{r^2}{J_{\mathrm{w}}}\right)\frac{\partial F_{\mathrm{x}}}{\partial \lambda}(\lambda_0)+\frac{F_{\mathrm{x}}}{m}(\lambda_0)\right] \tag{3.46}$$

and

$$\boldsymbol{B}_{\mathrm{b}} = \frac{r}{J_{\mathrm{w}}V_{\mathrm{x}}} \tag{3.47}$$

The first-order linear models will be used for the control designs of the PID and LQR in this thesis. The tire force F_x has been modeled with the Magic Formula model (3.10) by Pacejka. The complete expression for the linearized system with the tire force can be seen in Appendix A.

Frequency Domain Analysis

In the Figures 3.4 and 3.5 the Bode diagrams of the transfer functions of the system are shown during acceleration and braking. It is clear that the bandwidth of the system is degrading for increasing velocities. The range of velocities in the figures is between 1–27.78 m/s. This loss in bandwidth could be considered by gain scheduling (see Section 4.5) or some adaptive element in the control system.

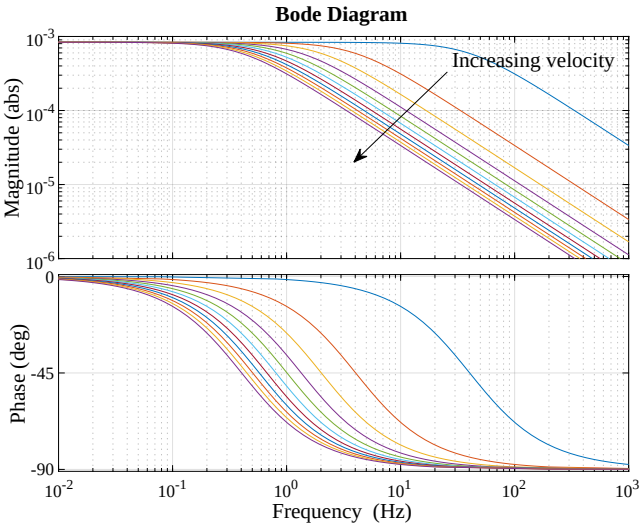

Figure 3.4: Bode diagram of transfer functions during acceleration, linearized at λ=0.08.

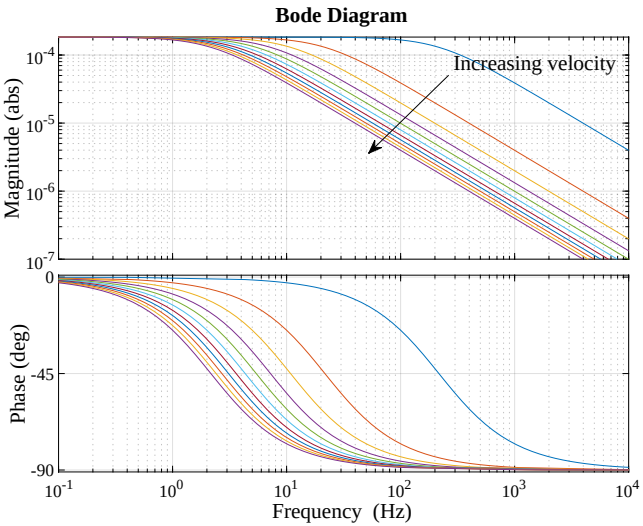

Figure 3.5: Bode diagram of transfer functions of the system during braking, linearized at λ=-0.02

4

Control Strategies

The purpose of this chapter is to briefly describe the different control strategies and concepts used throughout this thesis.

4.1 PID

Proportional integral derivative (PID) control, is the most commonly used control algorithm in the industry due to its simplicity and yet its good performance in a wide variety of systems and applications [Goodwin et al., 2000]. The algorithm is given by:

$$u = Ke(t) + \frac{K}{T_\mathrm{i}} \int_0^T e(t)dt + KT_\mathrm{d} \frac{de(t)}{dt} \tag{4.1}$$

where $e = r - y$ is the error between the reference signal r and the output signal y. The controller consists of three terms, a proportional term, an integral term and a derivative term. It is common that either the integral or the derivative part is excluded, i.e., the controller then becomes a PI or a PD. The control parameters are the proportional gain K and the integral and the derivative time constants T_i and T_d, respectively [Åström and Murray, 2020].

The proportional part acts on the current control error and can be applied to stabilize systems. The proportional part is, however, not sufficient to handle non-zero steady-state errors. By adding the integral term, the controller will counteract the steady-state error since the integral term is proportional to the accumulated error, i.e., it remembers the past error. The derivative term is acting on the rate of change of the control error, this makes the controller sensitive to high-frequency variations in the errors, which may be caused by measurement noise or fast reference changes. These fast changes in the error give large control outputs. In practice the PID controller is almost always implemented with derivative filtering and anti–windup compensation.

4.2 LQR

The idea behind the linear quadratic regulator is to find the control input $\boldsymbol{u} = -\boldsymbol{L}\boldsymbol{x}$, that minimizes the cost function J over an infinite time horizon [Hendricks et al., 2008]:

$$\text{minimize } J = \frac{1}{2}\int_0^\infty \boldsymbol{x}^T\boldsymbol{Q}\boldsymbol{x} + \boldsymbol{u}^T\boldsymbol{R}\boldsymbol{u}\, dt \tag{4.2}$$

$$\begin{aligned} \text{subject to} \quad \dot{\boldsymbol{x}} &= \boldsymbol{A}\boldsymbol{x} + \boldsymbol{B}\boldsymbol{u} \\ \boldsymbol{y} &= \boldsymbol{C}\boldsymbol{x} + \boldsymbol{D}\boldsymbol{u} \end{aligned} \tag{4.3}$$

where $\boldsymbol{x} \in \mathbb{R}^n$ is the system states and $\boldsymbol{u} \in \mathbb{R}^m$ is the input of the system. The matrix $\boldsymbol{A} \in \mathbb{R}^{n\times n}$ is the state transition matrix, $\boldsymbol{B} \in \mathbb{R}^{n\times m}$ is the input matrix, $\boldsymbol{C} \in \mathbb{R}^{p\times n}$ is the output matrix and $\boldsymbol{D} \in \mathbb{R}^{p\times n}$ is the direct coupling between the input and output, where it is assumed that $\boldsymbol{D} = \boldsymbol{0}$; $\mathbb{R}^n$ denoting the set of real-valued vectors of dimension n.

The weight matrix $\boldsymbol{Q}$ penalizes the state errors and is often chosen as a diagonal matrix and the weight matrix $\boldsymbol{R}$ penalizes the control input. The optimal control input $\boldsymbol{u}$ is found by solving the Riccati equation [Hendricks et al., 2008]. In order to solve the Riccati equation the system matrices $\boldsymbol{A}, \boldsymbol{B}$ must be stabilizable, the weight matrices $\boldsymbol{Q}$ and $\boldsymbol{R}$ must be positive definite and positive semi-definite, respectively, i.e., $\boldsymbol{Q} > \boldsymbol{0}$ and $\boldsymbol{R} \geq \boldsymbol{0}$. If these conditions are fulfilled, then there exists a positive definite matrix $\boldsymbol{P}$ that solves the Riccati equation:

$$\boldsymbol{0} = \boldsymbol{A}^T\boldsymbol{P} + \boldsymbol{P}\boldsymbol{A} + \boldsymbol{Q} - \boldsymbol{P}\boldsymbol{B}\boldsymbol{R}^{-1}\boldsymbol{B}^T\boldsymbol{P} \tag{4.4}$$

and the optimal input is given by:

$$\boldsymbol{u} = -\boldsymbol{L}\boldsymbol{x} = -\boldsymbol{R}^{-1}\boldsymbol{B}^T\boldsymbol{P}\boldsymbol{x} \tag{4.5}$$

Integral Action

In order to address steady-state errors, integral action can be added to the LQR. This could be done by extending the system model with an integral state $\boldsymbol{x}_\text{i} = \int_0^\infty (\boldsymbol{r} - \boldsymbol{C}\boldsymbol{x})dt$ [Åström and Murray, 2020]. The extended system then becomes:

$$\dot{\boldsymbol{x}}_\text{e} = \begin{bmatrix} \boldsymbol{A} & \boldsymbol{0} \\ -\boldsymbol{C} & \boldsymbol{0} \end{bmatrix}\boldsymbol{x}_\text{e} + \begin{bmatrix} \boldsymbol{B} \\ \boldsymbol{0} \end{bmatrix}\boldsymbol{u} + \begin{bmatrix} \boldsymbol{0} \\ \boldsymbol{I} \end{bmatrix}\boldsymbol{r} \tag{4.6}$$

$$\boldsymbol{y} = \begin{bmatrix} \boldsymbol{C} & \boldsymbol{0} \end{bmatrix}\boldsymbol{x}_\text{e} \tag{4.7}$$

where $\boldsymbol{x}_\text{e} = \begin{bmatrix} \boldsymbol{x}^T & \boldsymbol{x}_\text{i}^T \end{bmatrix}^T$. The control law is then obtained by solving the Riccati equation with the extended model. This gives the control law

$$\boldsymbol{u} = -\boldsymbol{L}_\text{e}\boldsymbol{x}_\text{e} = -\boldsymbol{L}\boldsymbol{x} - \boldsymbol{L}_\text{i}\boldsymbol{x}_\text{i} \tag{4.8}$$

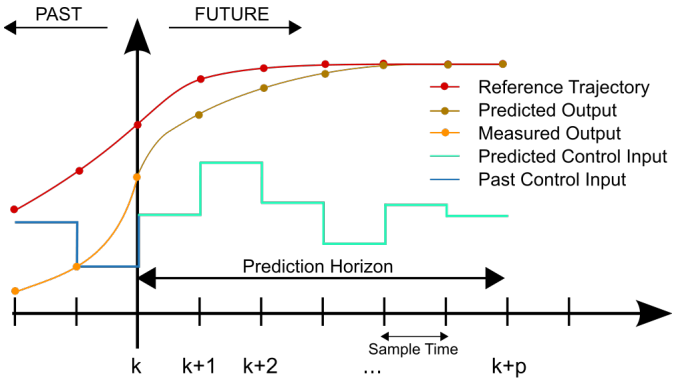

Figure 4.1: Concept of the receding horizon principle. Figure from [Behrendt, 2009]

4.3 MPC

Model predictive control (MPC) or receding horizon control, is a discrete time optimal control strategy [Rawlings et al., 2019]. The control output is obtained by first predicting the system's future behaviour based on a model of the system and the current states over a finite time horizon. Then based on these predictions, a sequence of control actions is obtained by solving an optimization problem online where only the first control action of the sequence is applied to the system. The time horizon is then shifted one step ahead in time. This is repeated at every sampling instant. The sequence of control actions is of open-loop form. Since the procedure is repeated every sample, a closed-loop effect is obtained. The advantage and main difference between MPC and LQR is that constraints on inputs, states and outputs can be handled by MPC. A possible disadvantage of MPC is the computational requirement that comes with solving the optimization problem online. An important requirement is a good model of the system in order to get a good performing controller.

The optimization problem is formulated by a cost function J_k, which is minimized with respect to the control input $\boldsymbol{u}_\mathrm{k}$. If the cost function is quadratic and the system and its constraints are linear, then the optimization problem to be solved is convex and if a solution exists it is a globally optimal solution to the problem. The optimal problem which is solved at every sampling instant can be formulated as

$$\underset{\boldsymbol{u}_\mathrm{k}}{\operatorname{argmin}} J_\mathrm{k} = \sum_{\mathrm{k}=0}^{\mathrm{p}} \left(\boldsymbol{x}_k^T \boldsymbol{Q}_\mathrm{k} \boldsymbol{x}_\mathrm{k} + \boldsymbol{x}_\mathrm{k}^T \boldsymbol{R}_\mathrm{k} \boldsymbol{u}_\mathrm{k}\right) + \boldsymbol{x}_{\mathrm{p}+1}^T \boldsymbol{Q}_\mathrm{f} \boldsymbol{x}_{\mathrm{p}+1} \tag{4.9}$$

$$\begin{aligned} \text{subject to} \quad & \boldsymbol{x}_{\mathrm{k}+1} = \Phi \boldsymbol{x}_\mathrm{k} + \Gamma \boldsymbol{u}_\mathrm{k} \\ & \boldsymbol{x}_\mathrm{k} \in \mathcal{X} \qquad \forall\, \mathrm{k} \in 0,..,\mathrm{p} \\ & \boldsymbol{u}_\mathrm{k} \in \mathcal{U} \qquad \forall\, \mathrm{k} \in 0,..,\mathrm{p} \end{aligned} \tag{4.10}$$

where $\boldsymbol{x}_\mathrm{k} \in \mathbb{R}^n$ and $\boldsymbol{u}_\mathrm{k} \in \mathbb{R}^m$. The constraints on the states and inputs are described by the sets $\mathcal{X}, \mathcal{U}$.

Successive Linearization

Successive linearization can be used in combination with MPC if the system is nonlinear and the controller is supposed to operate in a wide range of operating points [Basrah et al., 2017], [Zhakatayev et al., 2017]. One way to achieve this is to linearize the nonlinear system at the current operating points. An alternative is to linearize the nonlinear system around reference trajectories. In this thesis the successive linearization around the current operating point is used.

Consider the continuous-time nonlinear system (4.11) which is linearized around the points $(\boldsymbol{x}_\mathrm{l}, \boldsymbol{u}_\mathrm{l}) = (\boldsymbol{x}_\mathrm{k}, \boldsymbol{u}_{\mathrm{k}-1})$.

$$\dot{\boldsymbol{x}}_\mathrm{l} = \boldsymbol{f}(\boldsymbol{x}_\mathrm{l}, \boldsymbol{u}_\mathrm{l}) \tag{4.11}$$

The linear system obtained is then

$$\dot{\boldsymbol{x}} = \boldsymbol{A}\boldsymbol{x} + \boldsymbol{B}\boldsymbol{u} + \boldsymbol{K} \tag{4.12}$$

where

$$\boldsymbol{K} = \dot{\boldsymbol{x}}_\mathrm{l} - \boldsymbol{A}\boldsymbol{x}_\mathrm{l} - \boldsymbol{B}\boldsymbol{u}_\mathrm{l} \tag{4.13}$$

The linear system (4.12) is then discretized with a sample period T_s and the term K is seen as a piece-wise constant disturbance. This can be done by a simple approximation:

$$\frac{\boldsymbol{x}_{\mathrm{k}+1} - \boldsymbol{x}_\mathrm{k}}{T_\mathrm{s}} = \boldsymbol{A}\boldsymbol{x}_\mathrm{k} + \boldsymbol{B}\boldsymbol{u}_\mathrm{k} + \boldsymbol{K} \Rightarrow \tag{4.14}$$

$$\boldsymbol{x}_{\mathrm{k}+1} = (\boldsymbol{I} + \boldsymbol{A}T_\mathrm{s})\boldsymbol{x}_\mathrm{k} + \boldsymbol{B}T_\mathrm{s}\boldsymbol{u}_\mathrm{k} + \boldsymbol{K}T_\mathrm{s} \Rightarrow \tag{4.15}$$

$$\boldsymbol{x}_{\mathrm{k}+1} = \Phi\boldsymbol{x}_\mathrm{k} + \Gamma\boldsymbol{u}_\mathrm{k} + \boldsymbol{K}_\mathrm{k} \tag{4.16}$$

The obtained discrete-time linear system is then used for the predictions and in the solver. Other discretizations methods could be used if better numerical accuracy or stability is required, e.g., zero-order-hold discretization.

Integral Action

There are different approaches to include integral action in MPC. One alternative is to include the disturbances acting on the system in the model used in the MPC, then estimating the disturbances with a disturbance observer [Rawlings et al., 2019], (state estimation is discussed in Section 4.4). The model should reflect how the disturbances enter the system. Let the disturbances be denoted by $\boldsymbol{d}_\mathrm{k}$, then the linear model can be written as

$$\boldsymbol{x}_{\mathrm{k}+1} = \Phi\boldsymbol{x}_\mathrm{k} + \Gamma\boldsymbol{u}_k + \Gamma_\mathrm{d}\boldsymbol{d}_\mathrm{k} \tag{4.17}$$

$$\boldsymbol{y}_\mathrm{k} = \boldsymbol{C}\boldsymbol{x}_\mathrm{k} + \boldsymbol{C}_\mathrm{d}\boldsymbol{d}_\mathrm{k} \tag{4.18}$$

where $\boldsymbol{y}_\mathrm{k}$ is the measured outputs. $\Gamma_\mathrm{d} = \Gamma$ and $\boldsymbol{C}_\mathrm{d} = \boldsymbol{0}$ if the disturbance is expected to enter on the inputs of the system. If the disturbances are expected to enter on the outputs then $\Gamma_\mathrm{d} = \boldsymbol{0}$ and $\boldsymbol{C}_\mathrm{d} = \boldsymbol{I}$. Of course they can be used in combination in cases where the disturbances enter on both outputs and inputs of the system. The dimensions of the disturbances should match the number of measured outputs. In order to introduce integral action this way, the augmented system must be detectable, i.e., all unobservable states are stable. The augmented system is detectable if and only if the unaugmented system $(\Phi, \boldsymbol{C})$ is detectable and the following matrix has full rank:

$$\operatorname{rank} \begin{bmatrix} \boldsymbol{I} - \Phi & -\Gamma_\mathrm{d} \\ \boldsymbol{C} & \boldsymbol{C}_\mathrm{d} \end{bmatrix} = n + n_\mathrm{d} \tag{4.19}$$

where n, n_d is the number of states and number of disturbances entering the system, respectively.

4.4 Kalman Filter

It is not always possible to measure all the states that are needed for the controller due to costs of sensors, lack of space for installment of sensors or the states are measured but there is too much noise on the signals. This can be solved by using state estimation via a Kalman filter [Kalman, 1960], [Hendricks et al., 2008]. Consider the discrete-time linear system (4.20) where the system is exposed to Gaussian white noise on the input and the outputs:

$$\boldsymbol{x}_{\mathrm{k}+1} = \Phi \boldsymbol{x}_\mathrm{k} + \Gamma \boldsymbol{u}_\mathrm{k} + \boldsymbol{w}_\mathrm{k} \tag{4.20}$$

$$\boldsymbol{y}_\mathrm{k} = \boldsymbol{C}\boldsymbol{x}_\mathrm{k} + \boldsymbol{v}_\mathrm{k} \tag{4.21}$$

where the co-variances of $\boldsymbol{w}_\mathrm{k}$ and $\boldsymbol{v}_\mathrm{k}$ are $\mathrm{Cov}(\boldsymbol{w}_\mathrm{k}) = \boldsymbol{Q}$ and $\mathrm{Cov}(\boldsymbol{v}_\mathrm{k}) = \boldsymbol{R}$. The time–variant Kalman filter is a recursive algorithm and it can be divided in a prediction part and an update part. The estimated states $\hat{\boldsymbol{x}}$ are estimated with the algorithm given by [Chui and Chen, 2017]:
Predict:

$$\hat{\boldsymbol{x}}_{\mathrm{k}|\mathrm{k}-1} = \Phi_\mathrm{k} \hat{\boldsymbol{x}}_{\mathrm{k}-1|\mathrm{k}-1} + \Gamma_\mathrm{k} \boldsymbol{u}_\mathrm{k} \tag{4.22}$$

$$\boldsymbol{P}_{\mathrm{k}|\mathrm{k}-1} = \Phi_\mathrm{k} \boldsymbol{P}_{\mathrm{k}-1|\mathrm{k}-1} \Phi_\mathrm{k}^T + \boldsymbol{Q} \tag{4.23}$$

Update:

$$\hat{\boldsymbol{y}}_{\mathrm{k}} = \boldsymbol{C}\hat{\boldsymbol{x}}_{\mathrm{k|k-1}} \tag{4.24}$$

$$\boldsymbol{S}_{\mathrm{k}} = \boldsymbol{C}\boldsymbol{P}_{\mathrm{k|k-1}}\boldsymbol{C}^{T} + \boldsymbol{R} \tag{4.25}$$

$$\boldsymbol{K}_{\mathrm{k}} = \boldsymbol{P}_{\mathrm{k|k-1}}\boldsymbol{C}^{T}\boldsymbol{S}_{\mathrm{k}}^{-1} \tag{4.26}$$

$$\hat{\boldsymbol{x}}_{\mathrm{k|k}} = \hat{\boldsymbol{x}}_{\mathrm{k|k-1}} + \boldsymbol{K}_{\mathrm{k}}(\boldsymbol{y}_{\mathrm{k}} - \hat{\boldsymbol{y}}_{\mathrm{k}}) \tag{4.27}$$

$$\boldsymbol{P}_{\mathrm{k|k}} = (\boldsymbol{I} - \boldsymbol{K}_{\mathrm{k}}\boldsymbol{C})\boldsymbol{P}_{\mathrm{k|k-1}} \tag{4.28}$$

where the Φ_{k} and Γ_{k} may be time varying.

Disturbance Observer

Through the Kalman filter it is not only possible to estimate the states but it is also possible to estimate disturbances acting on the systems inputs or outputs [Rawlings et al., 2019], [Åström and Wittenmark, 2011]. This is done by augmenting the model (4.20) with a model of the disturbances. The augmented model now looks like:

$$\hat{\boldsymbol{x}}_{\mathrm{k+1}} = \Phi\hat{\boldsymbol{x}}_{\mathrm{k}} + \Gamma\boldsymbol{u}_{\mathrm{k}} + \Gamma_{\mathrm{d}}\hat{\boldsymbol{d}}_{\mathrm{k}} + \boldsymbol{w} \tag{4.29}$$

$$\hat{\boldsymbol{d}}_{\mathrm{k+1}} = \hat{\boldsymbol{x}}_{\mathrm{k}} + \boldsymbol{w}_{\mathrm{d}} \tag{4.30}$$

$$\hat{\boldsymbol{y}}_{\mathrm{k}} = \boldsymbol{C}\hat{\boldsymbol{x}}_{\mathrm{k}} + \boldsymbol{C}_{\mathrm{d}}\hat{\boldsymbol{d}}_{\mathrm{k}} + \boldsymbol{v} \tag{4.31}$$

where $\boldsymbol{w}_{\mathrm{d}}$ is white noise.

Extended Kalman Filter

If the system is nonlinear, a nonlinear model can be used instead in order to estimate the states [Chui and Chen, 2017]. In the extended Kalman filter the nonlinear model is linearized with a first-order Taylor-expansion. Consider the discrete-time nonlinear system:

$$\boldsymbol{x}_{\mathrm{k+1}} = \boldsymbol{f}(\boldsymbol{x}_{\mathrm{k}}, \boldsymbol{u}_{\mathrm{k}}) + \boldsymbol{w}_{\mathrm{k}} \tag{4.32}$$

$$\boldsymbol{y}_{\mathrm{k}} = \boldsymbol{h}(\boldsymbol{x}_{\mathrm{k}}) + \boldsymbol{v}_{\mathrm{k}} \tag{4.33}$$

The algorithm is similar in structure to the linear case, but the model in the predicting part is now instead nonlinear:
Predict:

$$\hat{\boldsymbol{x}}_{\mathrm{k|k-1}} = \boldsymbol{f}(\hat{\boldsymbol{x}}_{\mathrm{k-1|k-1}}, \boldsymbol{u}_{\mathrm{k-1}}) \tag{4.34}$$

$$\boldsymbol{P}_{\mathrm{k|k-1}} = \Phi_{\mathrm{k}}\boldsymbol{P}_{\mathrm{k-1|k-1}}\Phi_{\mathrm{k}}^{T} + \boldsymbol{Q} \tag{4.35}$$

Update:

$$\hat{\boldsymbol{y}}_{\mathrm{k}} = \boldsymbol{C}\hat{\boldsymbol{x}}_{\mathrm{k|k-1}} \tag{4.36}$$

$$\boldsymbol{S}_{\mathrm{k}} = \boldsymbol{C}\boldsymbol{P}_{\mathrm{k|k-1}}\boldsymbol{C}^{T} + \boldsymbol{R} \tag{4.37}$$

$$\boldsymbol{K}_{\mathrm{k}} = \boldsymbol{P}_{\mathrm{k|k-1}}\boldsymbol{C}^{T}\boldsymbol{S}_{\mathrm{k}}^{-1} \tag{4.38}$$

$$\hat{\boldsymbol{x}}_{\mathrm{k|k}} = \hat{\boldsymbol{x}}_{\mathrm{k|k-1}} + \boldsymbol{K}_{\mathrm{k}}(\boldsymbol{y}_{\mathrm{k}} - \hat{\boldsymbol{y}}_{\mathrm{k}}) \tag{4.39}$$

$$\boldsymbol{P}_{\mathrm{k|k}} = (\boldsymbol{I} - \boldsymbol{K}_{\mathrm{k}}\boldsymbol{C})\boldsymbol{P}_{\mathrm{k|k-1}} \tag{4.40}$$

The disturbance observer and the extended Kalman filter can be combined in a similar way as in the linear case.

4.5 Gain Scheduling

Most physical systems are nonlinear in their nature and their dynamics change depending on operating conditions. This may lead to inefficient or even unstable controllers if the dynamics differ too much compared to the conditions the controller was designed for initially. One way to accommodate this issue is to use gain scheduling [Åström and Wittenmark, 2008]. In gain scheduling the parameters in the controller are changed depending on the current operating conditions, see Figure 4.2. These parameters are computed offline and they are often selected using a look-up table. The selection is made by measuring some suitable variables which reflect the current operating conditions.

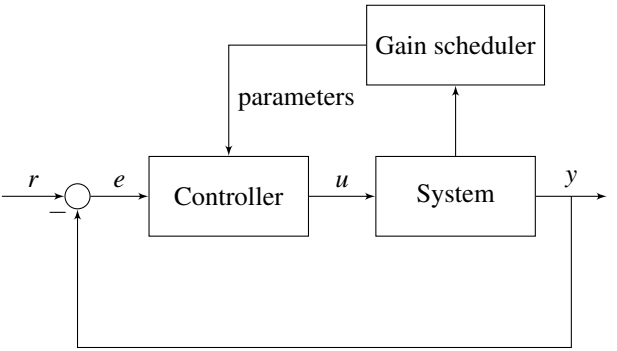

Figure 4.2: Block diagram of a feedback system with gain scheduling.

5

Control Design & Tuning

In this section the choice, design and the tuning process of the controllers used in the simulations are presented. Stability and robustness of the controllers will be analysed. The controllers are tested through simulations in Chapter 6.

5.1 Requirements

In the process of designing and tuning the controllers it has been important that the controllers can handle different disturbances, be robust against model errors and parameter uncertainties.

Model errors and disturbances are handled through integral action. The different methods discussed in Chapter 4 have been used for the respective controller.

The robustness of and stability of the controllers have been analyzed through frequency and step response based on the gang of four [Åström and Murray, 2020]:

$$\begin{aligned} S(s) &= \frac{1}{1+G_{\mathrm{p}}(s)G_{\mathrm{c}}(s)}, & T(s) &= \frac{G_{\mathrm{p}}(s)G_{\mathrm{c}}(s)}{1+G_{\mathrm{p}}(s)G_{\mathrm{c}}(s)} \\ P(s)S(s) &= \frac{G_{\mathrm{p}}(s)}{1+G_{\mathrm{p}}(s)G_{\mathrm{c}}(s)}, & C(s)S(s) &= \frac{G_{\mathrm{c}}(s)}{1+G_{\mathrm{p}}(s)G_{\mathrm{c}}(s)} \end{aligned} \tag{5.1}$$

where $S(s)$ is the sensitivity function, $T(s)$ the complementary function, $P(s)S(s)$ is the load sensitivity function and the noise sensitivity function is $C(s)S(s)$. $G_p(s)$ and $G_c(s)$ are the transfer functions of the system and the controller, respectively. The transfer functions have been derived from Figure 5.1. The sensitivity function $S(s)$ is the transfer function between the signals n and y. The complementary function $T(s)$ is the transfer function between the signals r and y. The noise sensitivity function $C(s)S(s)$ and the load sensitivity function $P(s)S(s)$ are the transfer functions between the signals n, d and d, y, respectively.

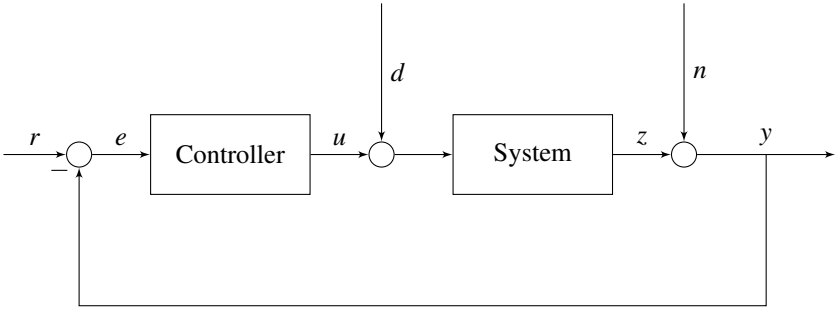

Figure 5.1: Block diagram of a one degree of freedom feedback system.

5.2 PID

The PID controller was chosen since it is the most common controller used in industry. The controller is also relatively easy to implement in software. In this thesis a PI controller was designed and tested through simulations and later also in experiments (see Chapter 7 and Chapter 8).

Tuning

The PI controller given by Equation 4.1 was tuned partially according to the method used in [Vasiljevic et al., 2012]. The integral time T_i was chosen to the open–loop time constant, τ of the system, i.e., $T_\mathrm{i} = \tau$. The proportional gain K was tuned iteratively until a desired performance was achieved. In Table 5.1 the chosen PI parameters are shown. The choice of PI parameters gives the closed-loop transfer function:

$$G_\mathrm{cl}(s) = \frac{G_\mathrm{p}(s)G_\mathrm{PID}(s)}{1+G_\mathrm{p}(s)G_\mathrm{PID}(s)} = \frac{K\beta}{s+K\beta} \tag{5.2}$$

where

$$G_\mathrm{p}(s) = \frac{\beta}{s+\alpha} = \frac{\beta/\alpha}{1+\frac{1}{\alpha}s} = \frac{\beta\tau}{1+\tau s} \tag{5.3}$$

and

$$G_\mathrm{PID}(s) = K(1+\frac{1}{sT_\mathrm{i}}) = K\frac{(sT_\mathrm{i}+1)}{sT_\mathrm{i}} = K\frac{(s\tau+1)}{s\tau} \tag{5.4}$$

Frequency Domain Analysis

Figures 5.2 and 5.3 show the Bode diagram and the step response of the gang of four for the PI controller in the acceleration case. By looking at the Bode diagram for the transfer function $C(s)S(s)$ it shows that the controller is sensitive for low-frequency disturbances between the output and the input of the system. The same

Table 5.1: PI parameters used in the simulations.

PI Parameters		
Parameter	**Acceleration**	**Braking**
K:	50.0	30.0
T_i:	0.004	0.0007

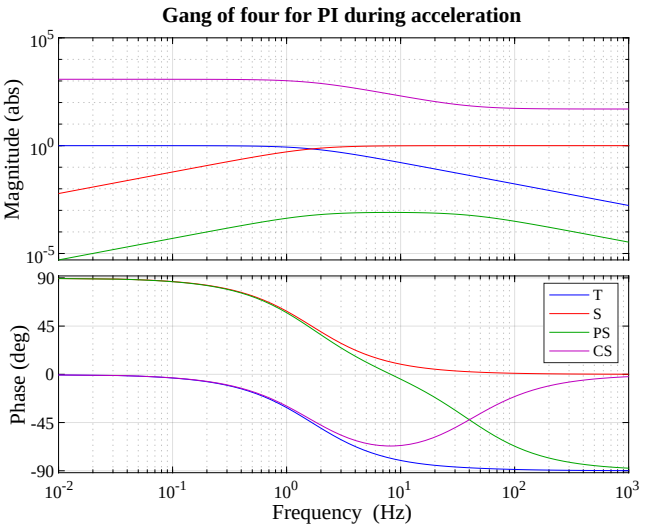

Figure 5.2: Bode diagram of the gang of four for the PI controller during acceleration, linearized at the slip ratio $\lambda = 0.08$.

sensitivity is seen in the corresponding step response.

Figures 5.4 and 5.5 show the Bode diagram and the step response of the gang of four for the PI controller in the braking case. The Bode diagram shows the same sensitivity for low-frequency disturbances as for the acceleration case, although with a bit higher gain.

5.3 LQR

The LQR was chosen since there exist good systematic methods to tune this type of controller. The controller is also relatively simple to implement. Since the states often represent some physical quantity the tuning process can be a bit more intuitive

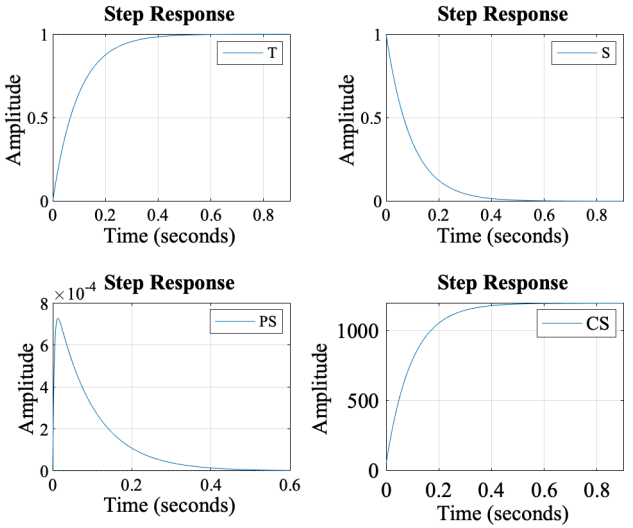

Figure 5.3: Step response of the gang of four for the PI controller during acceleration.

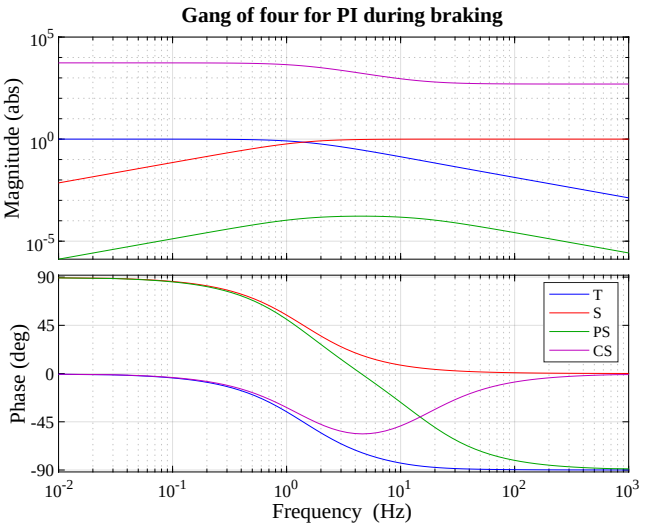

Figure 5.4: Bode diagram of the gang of four for the PI controller during braking, linearized at the slip ratio $\lambda = -0.02$.

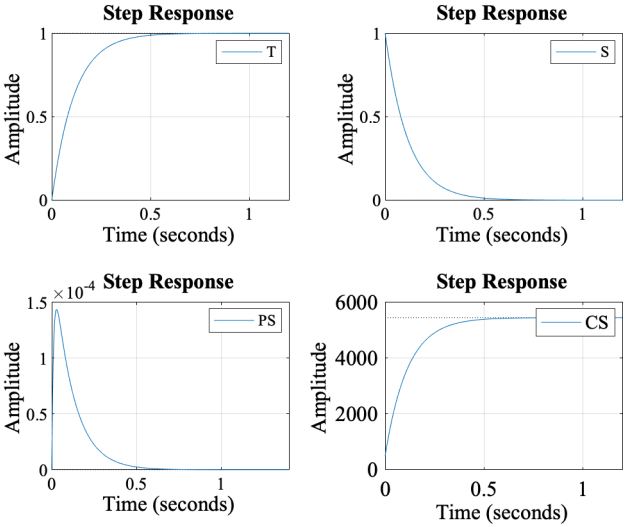

Figure 5.5: Step response of the gang of four for the PI controller during braking.

compared to the PI tuning.

Tuning

The LQR was designed based on the linear models derived in Chapter 3, where integral action was added in order to address steady-state errors according to Chapter 4. The LQR gains were obtained by choosing the weights Q and R according to:

$$\boldsymbol{Q} = \begin{pmatrix} \frac{1}{x_{\text{max}}^2} & 0 \\ 0 & \frac{1}{x_{\text{i,max}}^2} \end{pmatrix}, \qquad \boldsymbol{R} = \frac{1}{u_{\text{max}}^2} \tag{5.5}$$

where x_{max} is the maximal deviation from the desired setpoint, x_i is the maximal integral action and u_{max} is the maximal allowed control input. This method was used as a starting point and the weights were then tuned iteratively until desired performance was obtained. In Table 5.2 the chosen weights are shown.

Frequency Domain Analysis

Figures 5.6, 5.7, 5.8 and 5.9 show the Bode diagrams and the step responses of the complementary & sensitivity function for the LQR in the acceleration and the braking cases.

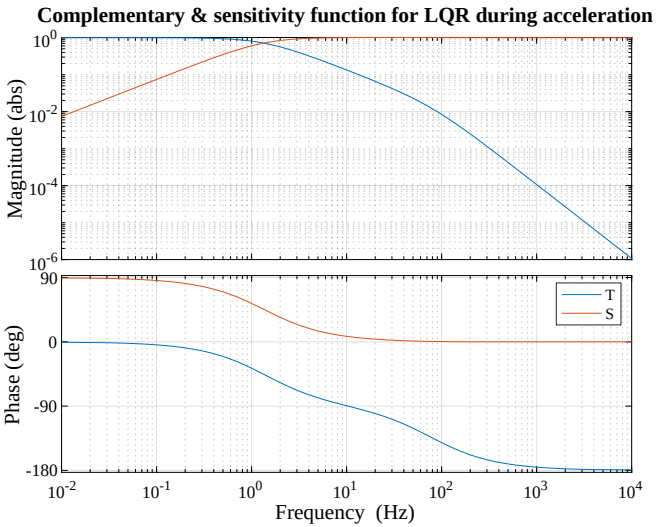

Figure 5.6: Bode diagram of the complementary & sensitivity function for the LQR controller during acceleration, linearized at the slip $\lambda = 0.08$.

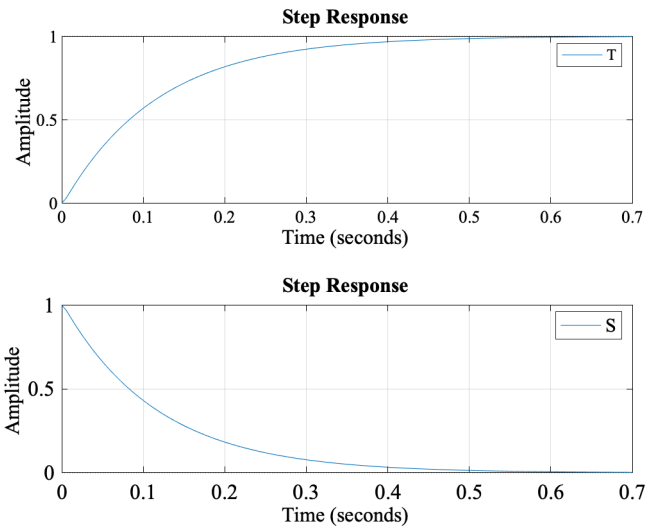

Figure 5.7: Step response of the complementary & sensitivity function for the LQR controller during acceleration.

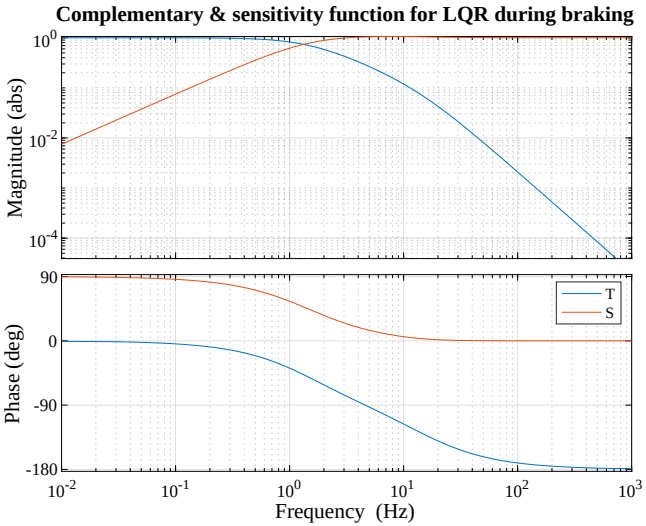

Figure 5.8: Bode diagram of the complementary & sensitivity function for the LQR controller during braking, linearized at the slip ratio $\lambda = -0.02$.

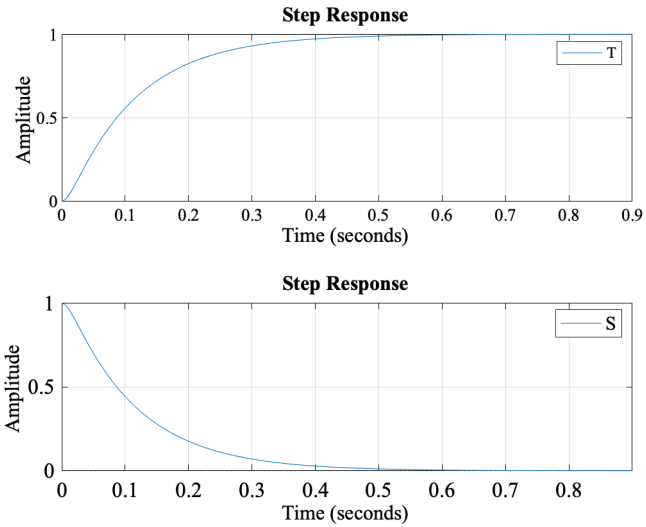

Figure 5.9: Step response of the complementary & sensitivity function for the LQR controller during braking.

Table 5.2: LQR weights used in the simulations.

LQR - Weights		
Parameter	**Acceleration**	**Braking**
$x_{\max}$:	0.1	1.0
$x_{\mathrm{i,max}}$:	0.01	0.01
$u_{\max}$:	200.0	-100.0

5.4 MPC

The MPC was chosen as the third control design alternative since it can handle constraints on, e.g., inputs and outputs.

Tuning

For the MPC design the nonlinear second-order models with velocity dynamics derived in Chapter 3 were used:

Acceleration

$$\dot{V}_{\mathrm{x}} = \frac{1}{m} F_{\mathrm{xr}} \tag{5.6}$$

$$\dot{\lambda}_{\mathrm{a}} = -\frac{1}{V_{\mathrm{x}}} \left(\frac{1-\lambda}{m} + r^2 \frac{(1-\lambda)^2}{J_{\mathrm{w}}} \right) F_{\mathrm{x}} + \frac{r(1-\lambda)^2}{J_{\mathrm{w}} V_{\mathrm{x}}} (T_{\mathrm{m}} - T_{\mathrm{b}}) \tag{5.7}$$

Braking

$$\dot{V}_{\mathrm{x}} = \frac{1}{m} F_{\mathrm{xr}} \tag{5.8}$$

$$\dot{\lambda}_{\mathrm{b}} = -\frac{1}{V_{\mathrm{x}}} \left(\frac{1+\lambda}{m} + \frac{r^2}{J_{\mathrm{w}}} \right) F_{\mathrm{x}} + \frac{r}{J_{\mathrm{w}} V_{\mathrm{x}}} (T_{\mathrm{m}} - T_{\mathrm{b}}) \tag{5.9}$$

These models are linearized successively around the current states and the previous inputs as discussed in Chapter 4. The linear system obtained is then discretized through the Euler approximation. Integral action was also added in order to handle steady-state errors by augmenting the model with a disturbance acting on the input, which in turn is estimated through an extended Kalman filter as discussed in Chapter 4.

The constraints on the input are described by the set $\mathcal{U}$. The chosen MPC parameters are shown in Table 5.3. The sample frequency was set to $f_{\mathrm{s}} = 100$ Hz. The prediction horizon p was set to 25 and the input constraints were set to 360 Nm and -200 Nm for the acceleration and braking case, respectively. It should be noted that the available torque on the real motor is unknown. The chosen torque constraints are probably set a bit high compared to the real vehicle. No constraints on the states were chosen.

Table 5.3: MPC weights used in the simulations.

MPC - Weights		
Parameter	**Acceleration**	**Braking**
Q_1:	1.0×10^{-4}	1.0×10^{-4}
Q_2:	10.0×10^{6}	10.0×10^{6}
R:	1.0×10^{-6}	1.0×10^{-6}
Q_{f1}:	1.0×10^{-8}	1.0×10^{-6}
Q_{f2}:	1.0×10^{6}	25.0×10^{4}
f_s:	100 Hz	100 Hz
p:	25	25
$\mathcal{U}$	$0 \leq u_k \leq 360$	$-200 \leq u_k \leq 0$

Table 5.4: EKF weights used in the simulations.

EKF - Weights		
Parameter	**Acceleration**	**Braking**
Q_1:	1.0×10^{3}	1.0×10^{3}
Q_2:	10.0×10^{3}	10.0×10^{3}
Q_3:	10.0×10^{9}	10.0×10^{9}
R:	0.0001	0.1
f_s	250 Hz	250 Hz

EKF

In order to estimate the disturbances acting on the system, an extended Kalman filter combined with a disturbance observer was designed as discussed in Chapter 4. The nonlinear models (5.6) and (5.8) are discretized with a sample frequency f_s at every sample instant with Euler approximation. Table 5.4 shows the chosen filter parameters.

6

Simulations

In this chapter the driving scenarios and test conditions are presented. Results of the simulations of the controllers are also presented and discussed. All simulations were made and implemented in MATLAB/Simulink.

6.1 Simulation Scenarios

The controllers were simulated against the nonlinear models (5.6) and (5.8) for the acceleration case and for the braking case, respectively. All simulations during acceleration were made with an initial velocity of 3.6 km/h (1 m/s) and all the braking simulations were made from an initial velocity of 54 km/h (15 m/s). It was also assumed that acceleration and braking occur along a straight line. Different tests were performed in simulations. All controllers were tuned for parameter set Dry asphalt 1. In all simulation tests the controllers were tested against the nonlinear models with parameter set Dry asphalt 1 unless otherwise stated.

Test 1: In the first test the controllers were tuned for the parameter set Dry asphalt 1 which could be considered as a reference test under ideal conditions. The controllers were tested against the nonlinear models with the same parameter set.

Test 2: In the second test the controllers were tuned for the same parameter set as in Test 1. The controllers were tested against the nonlinear models with the parameter set Dry asphalt 2. This test were intended to test robustness against parameter uncertainties.

Test 3: In the third test the controllers' disturbance rejection were tested, where a disturbance of - 50 Nm was applied to the input of the system at time $t = 3$ seconds. This was supposed to simulate a scenario where a braking force is applied to the system.

Test 4: In the fourth test the controllers' noise sensitivity were tested where white noise with a variance $\sigma^2 = 0.001$ was injected at the wheel speed measurement.

Table 6.1: Parameters used in the models for the simulations.

Model Parameters	
Mass m:	120 kg
Inertia J:	1 kg m^2
Radius of rear wheel r:	0.25 m
Gravity g:	9.8 m/s^2

Table 6.2: Magic Formula coefficients used in the simulations.

Magic Formula Coefficients						
Surface	B	C	D	E	S_h	S_v
Dry asphalt 1	10.0	1.9	1.0	0.97	0.0	0.0
Dry asphalt 2	19.25	1.65	0.92	0.0	0.0	0.0
Wet asphalt	12.0	2.3	0.82	1.0	0.0	0.0

Test 5: A fifth simulation test where the road conditions were suddenly changed from the dry asphalt to wet asphalt was made to test how the controllers and the system react to transients. The parameter sets used in this test was Dry asphalt 1 and Wet asphalt. The change in road conditions happens at time $t = 3$ seconds.

Table 6.1 shows the parameters for the vehicle used in the simulations. Table 6.2 shows the different parameters used in the simulations and Figure 6.1 shows the corresponding slip curve for each parameter set.

6.2 Results

In this section the simulation results of the three controllers, PI, LQR and MPC, are presented.

PID

Acceleration: Figure 6.2 shows the results of the PI controller during acceleration with two different parameter sets for dry asphalt, i.e., *Test 1* and *Test 2*. The results are similar although there can be seen some overshoot in the slip for the parameter set Dry asphalt 2, see Figure 6.2d. The controller seems to be robust against some parameter uncertainty. Figure 6.3 shows two scenarios with different disturbances acting on the system. In Figures 6.3a, 6.3c and 6.3e the result of *Test 3* is shown. The controller's response is fast and counteracts the disturbance by increasing the driving torque.

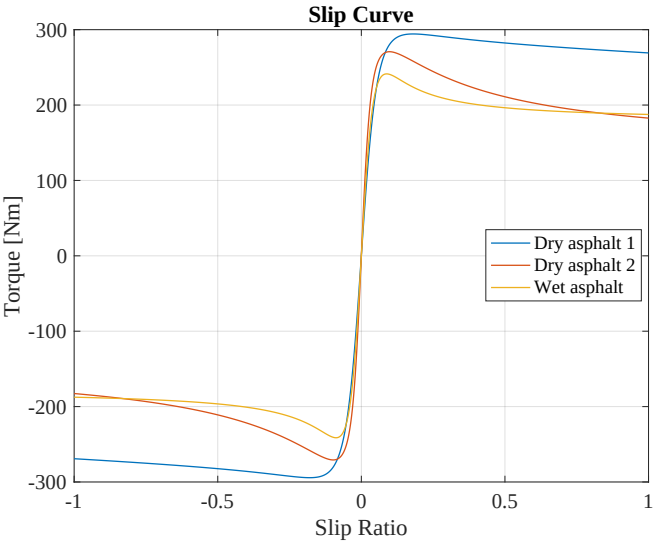

Figure 6.1: Slip curve corresponding to the Magic Formula coefficients in Table 6.2

Figures 6.3b, 6.3d and 6.3f show results of *Test 4* The noise is very apparent in the slip for lower velocities.

In Figure 6.4 the results of *Test 5* is shown. There is an initial transient after the conditions are changed and it takes about 3 seconds before the controller has settled to the reference again. The controller responds by decreasing the applied torque. The controller for this tuning seems to be sensitive to such disturbances.

Braking: Figure 6.5 shows the results of the PI controller during braking with two different parameter sets for dry asphalt, i.e., *Test 1* and *Test 2*. The results are similar for the two different sets. The controller in the braking case seems also to handle some parameter uncertainty to some degree. Figure 6.6 shows two scenarios with different disturbances acting on the system. Figures 6.6a, 6.6c and 6.6e show the result of *Test 3*. The controller's response is fast and counteracts the disturbance by decreasing the braking torque.

Figures 6.6b, 6.6d and 6.6f show results of *Test 4*. The noise is very apparent in the slip for lower velocities. Figure 6.7 the result of *Test 5* is shown. There is an initial transient but the controller settles in to the reference fastly by increasing the braking torque. The peaks which appear in Figures 6.5c, 6.5d, 6.6c and 6.7b are due to the velocity approaching 0 km/h. The increase of noise at the end of the simulation after $t = 5$ seconds in Figure 6.6d is due to the velocity approaching 0 km/h, the system is sensitive for noise at lower velocities.

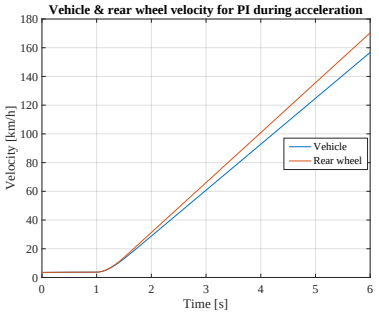

(a) **Test 1:** Vehicle & wheel velocity.

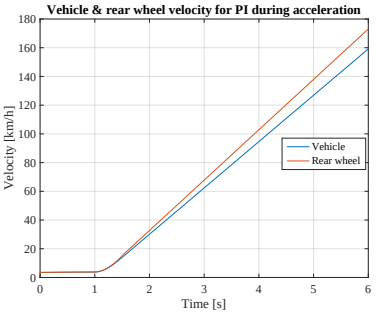

(b) **Test 2:** Vehicle & wheel velocity.

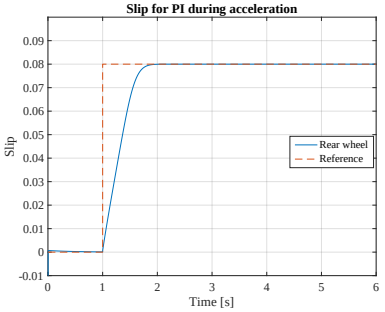

(c) **Test 1:** Slip.

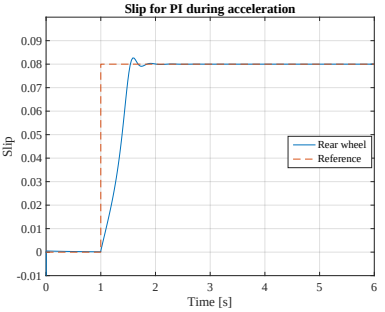

(d) **Test 2:** Slip

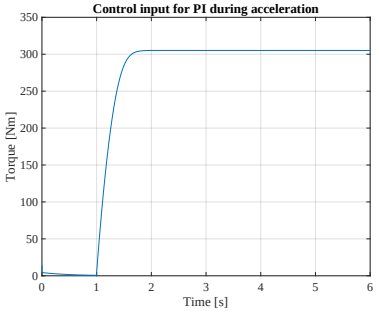

(e) **Test 1:** Control input.

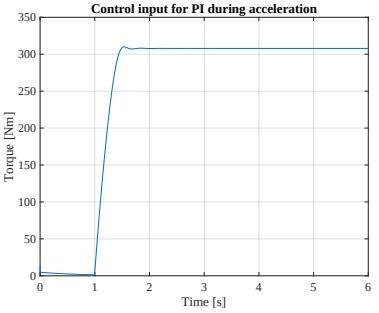

(f) **Test 2:** Control input.

Figure 6.2: Simulation with the PID controller during acceleration for two different parameter sets for dry asphalt, Dry asphalt 1 (left) and Dry asphalt 2 (right). The controller is tuned for Dry asphalt 1.

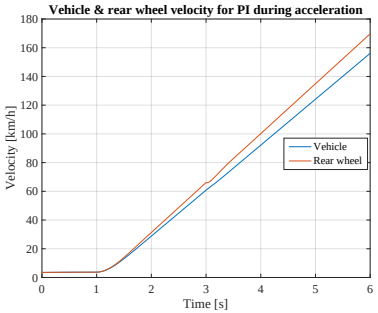

(a) **Test 3:** Vehicle & wheel velocity with a step disturbance on the control input.

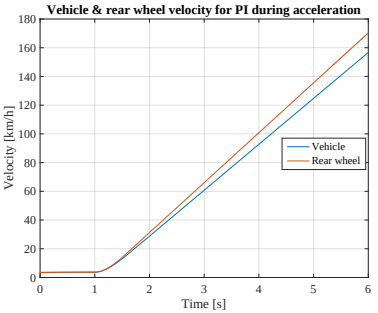

(b) **Test 4:** Vehicle & wheel velocity with noise added on the wheel velocity output.

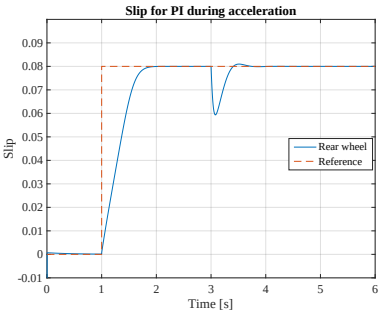

(c) **Test 3:** Slip with a step disturbance on the control input.

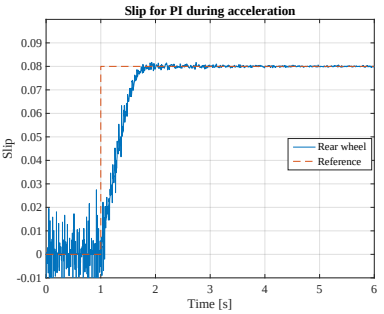

(d) **Test 4:**Slip with noise added on the wheel velocity output.

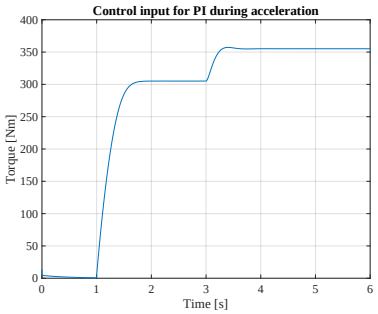

(e) **Test 3:** Control input with a step disturbance on the control input.

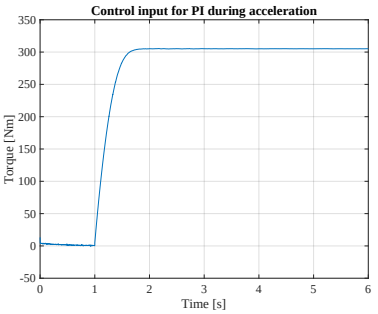

(f) **Test 4:** Control input with noise added on the wheel velocity output.

Figure 6.3: Simulation with the PID controller during acceleration with a step disturbance of -50 Nm on the input (left) and white noise added on the rear wheel velocity with a variance of 0.001 (right).

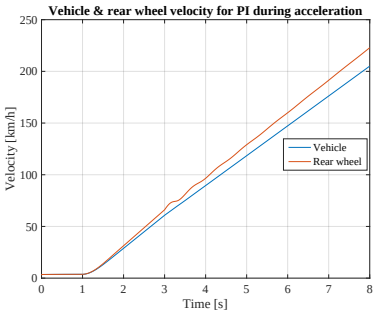

(a) **Test 5:** Vehicle & wheel velocity with changing road conditions.

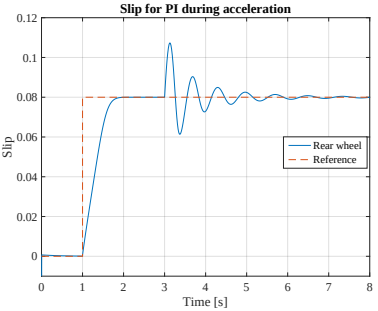

(b) **Test 5:** Slip with changing road conditions.

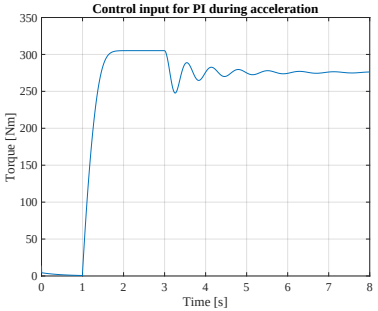

(c) **Test 5:** Control input with changing road conditions.

Figure 6.4: Simulation with the PID controller during acceleration with changing road conditions from dry asphalt to wet asphalt at $t = 3$ seconds.

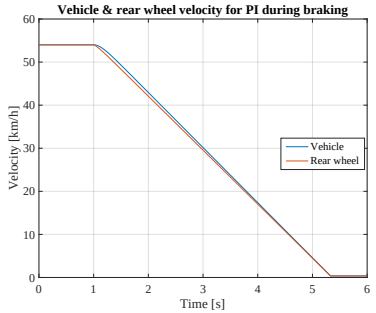

(a) **Test 1:** Vehicle & wheel velocity.

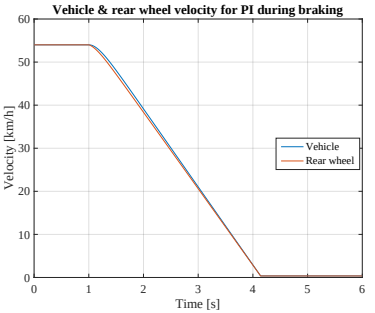

(b) **Test 2:** Vehicle & wheel velocity.

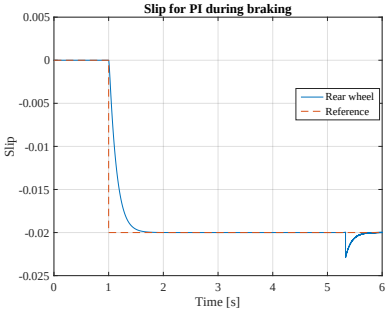

(c) **Test 1:** Slip.

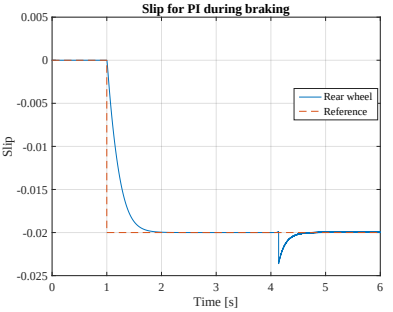

(d) **Test 2:** Slip

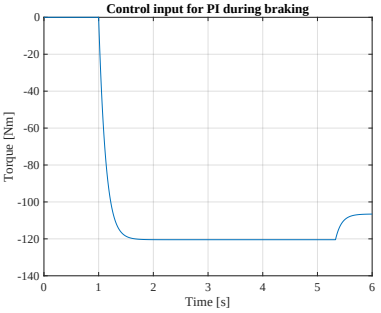

(e) **Test 1:** Control input.

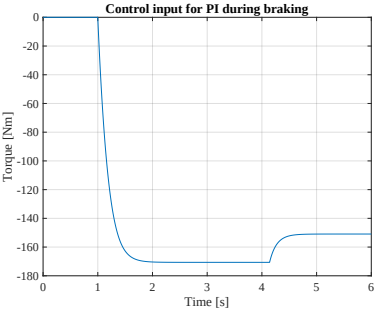

(f) **Test 2:** Control input.

Figure 6.5: Simulation with the PID controller during braking for two different parameter sets for dry asphalt, Dry asphalt 1 (left) and Dry asphalt 2 (right). The controller is tuned for parameter set Dry asphalt 1.

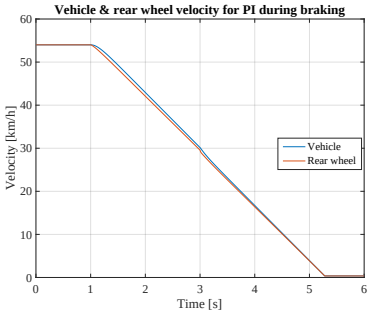

(a) **Test 3:** Vehicle & wheel velocity with a step disturbance on the control input.

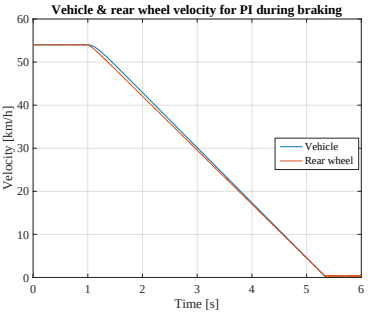

(b) **Test 4:** Vehicle & wheel velocity with noise added on the wheel velocity output.

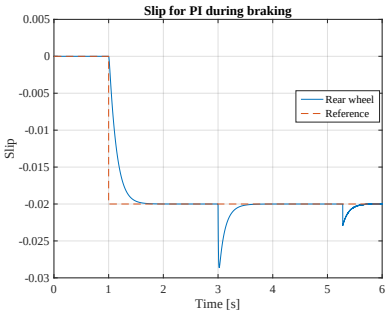

(c) **Test 3:** Slip with a step disturbance on the control input.

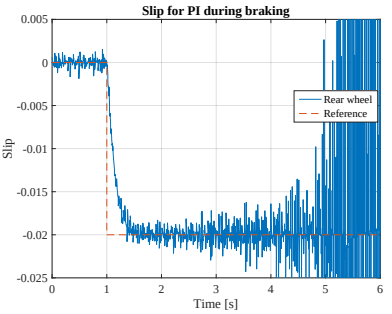

(d) **Test 4:** Slip with noise added on the wheel velocity output.

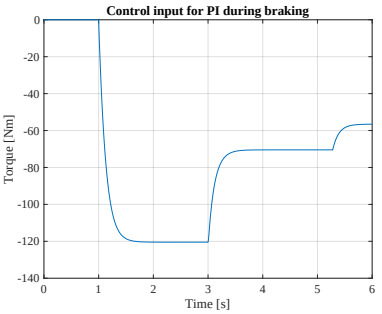

(e) **Test 3:** Control input with a step disturbance on the control input.

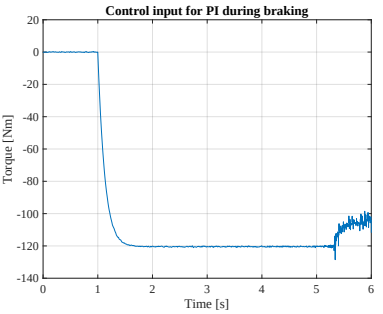

(f) **Test 4:** Control input with noise added on the wheel velocity output.

Figure 6.6: Simulation with the PID controller during braking with a step disturbance of -50 Nm on the input (left) and white noise added on the rear wheel velocity with a variance of 0.001 (right).

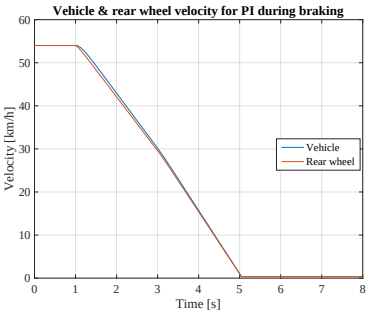

(a) **Test 5:** Vehicle & wheel velocity with changing road conditions.

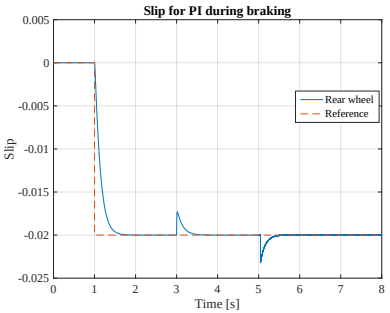

(b) **Test 5:** Slip with changing road conditions.

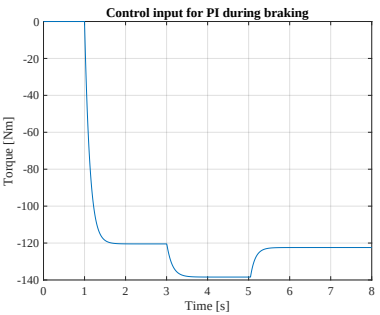

(c) **Test 5:** Control input with changing road conditions.

Figure 6.7: Simulation with the PID controller during braking with changing road conditions from dry asphalt to wet asphalt at $t = 3$ seconds.

LQR

Acceleration: Figure 6.8 shows the results of the LQR controller during acceleration with two different parameter sets for dry asphalt, i.e., *Test 1* and *Test 2*. The results are very similar in both cases and the controller seems to be robust against some parameter uncertainty for this tuning.

Figure 6.9 shows two scenarios with different disturbances acting on the system. In Figures 6.9a, 6.9c and 6.9e the result of *Test 3* is shown. The controller's response is fast and counteracts the disturbance by increasing the driving torque. Figures 6.9b, 6.9d and 6.9f show results of *Test 4*. The noise is very apparent in the slip for lower velocities and the noise can also be seen affecting the control signal.

In Figure 6.10 the result of *Test 5* is shown. There is an initial transient in the slip after the conditions are changed, but the controller is responding fast for the changed conditions by decreasing the applied torque.

Braking: Figure 6.11 shows the results of the LQR controller during braking with two different parameter sets for dry asphalt, *Test 1* and *Test 2*. The controller is able to decelerate faster for the parameter set Dry asphalt 2.

Figure 6.12 shows two scenarios with different disturbances acting on the system. In Figures 6.12a, 6.12c and 6.12e the result of *Test 3* is shown. The controller's response is fast and counteracts the disturbance by increasing the driving torque.

Figures 6.12b, 6.12d and 6.12f show results of *Test 4*. The noise is very apparent in the slip for lower velocities. As in the acceleration case, the noise is clearly seen affecting the control input too.

In Figure 6.13c the result of *Test 5* is shown. There is an initial transient in the slip after the road conditions are changed, and the controller responds by increasing the applied torque. The peaks which appear in Figures 6.11c, 6.11d, 6.12c and 6.13b are due to the velocity v approaching 0 km/h. The increase of noise at the end of the simulation after $t = 5$ seconds in Figure 6.12d is due to the velocity v approaching 0 km/h, the system is sensitive for noise at lower velocities.

MPC

Acceleration: Figure 6.14 shows the results of the MPC controller during acceleration with two different parameter sets for dry asphalt, i.e., *Test 1* and *Test 2*. The results are very similar in both cases and the controller seems to be robust against some parameter uncertainty. In Figure 6.14d there is some overshoot in the slip, but it is acceptable.

Figure 6.15 shows two scenarios with different disturbances acting on the system. In Figures 6.15a, 6.15c and 6.15e the result of *Test 4* is shown. The controller's response is fast and counteracts the disturbance by increasing the driving torque.

Figures 6.15b, 6.15d and 6.15f show results of *Test 4*. The noise is very apparent in the slip for lower velocities, but the noise can also be seen affecting the control input signal. In Figure 6.15f the noise on the control input is more apparent compared to the PID and the LQR.

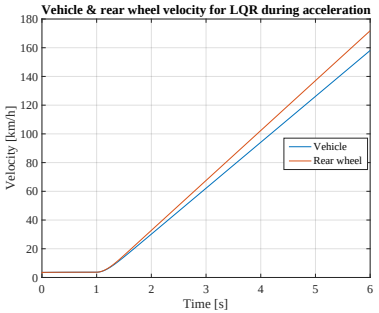

(a) **Test 1:** Vehicle & wheel velocity.

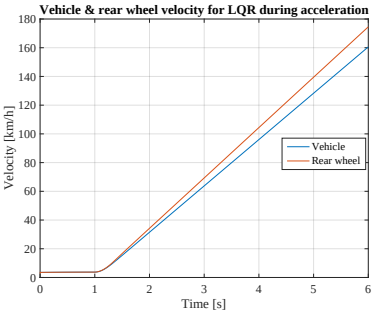

(b) **Test 2:** Vehicle & wheel velocity.

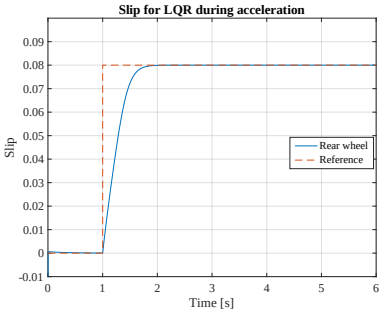

(c) **Test 1:** Slip.

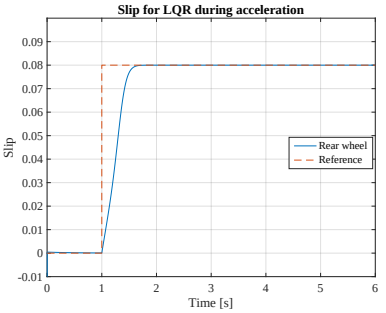

(d) **Test 2:** Slip

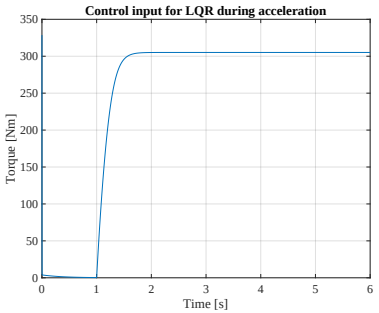

(e) **Test 1:** Control input.

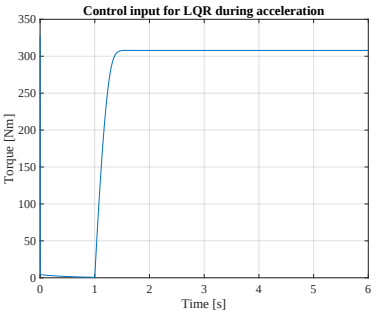

(f) **Test 2:** Control input.

Figure 6.8: Simulation with the LQR controller during acceleration for two different parameter sets for dry asphalt, Dry asphalt 1 (left) and Dry asphalt 2 (right). The controller is tuned for the parameter set Dry asphalt 1.

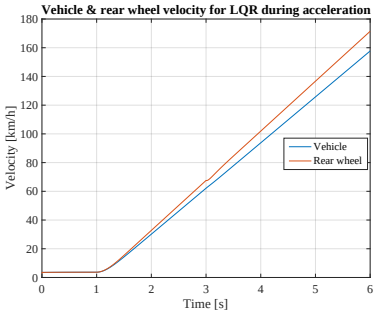

(a) **Test 3:** Vehicle & wheel velocity with a step disturbance on the control input.

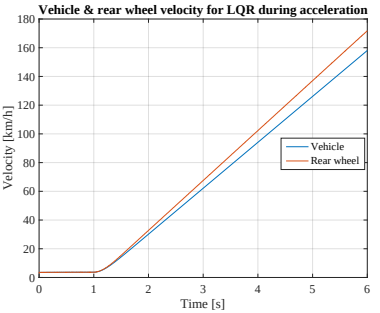

(b) **Test 4:** Vehicle & wheel velocity with noise added on the wheel velocity output.

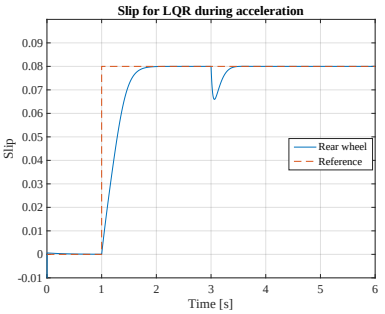

(c) **Test 3:** Slip with a step disturbance on the control input.

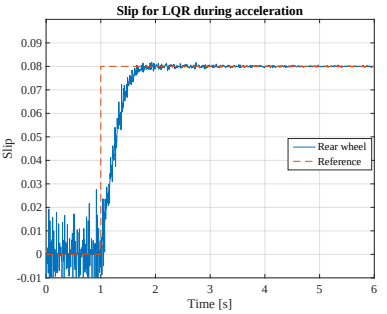

(d) **Test 4:** Slip with noise added on the wheel velocity output.

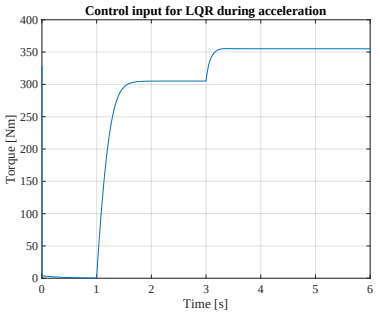

(e) **Test 3:** Control input with a step disturbance on the control input.

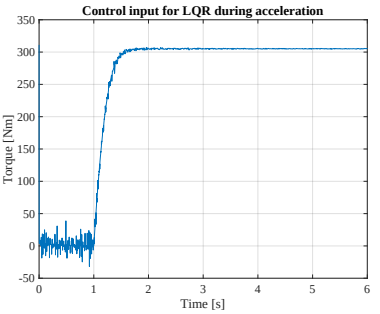

(f) **Test 4:** Control input with noise added on the wheel velocity output.

Figure 6.9: Simulation with the LQR controller during acceleration with a step disturbance of -50 Nm on the input (left) and white noise added on the rear wheel velocity with a variance of 0.001 (right).

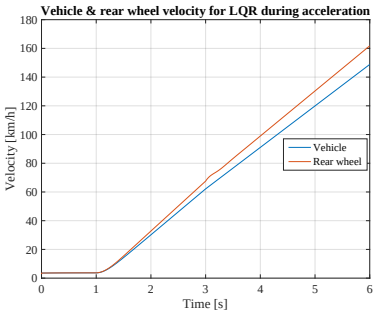

(a) **Test 5:** Vehicle & wheel velocity with changing road conditions.

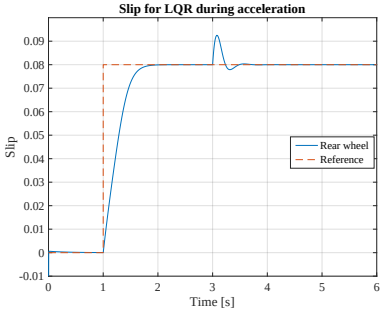

(b) **Test 5:** Slip with changing road conditions.

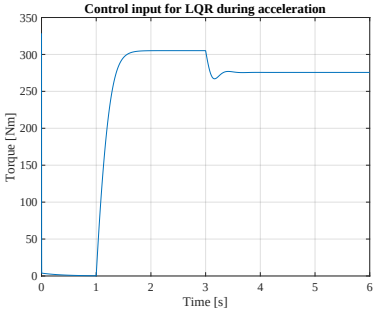

(c) **Test 5:** Control input with changing road conditions.

Figure 6.10: Simulation with the LQR controller during acceleration with changing road conditions from dry asphalt to wet asphalt at $t = 3$ seconds.

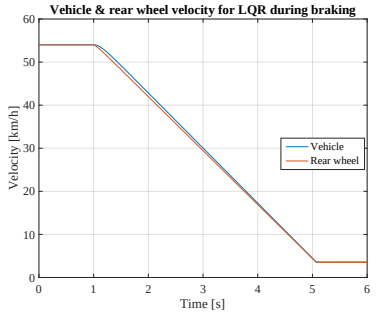

(a) **Test 1:** Vehicle & wheel velocity.

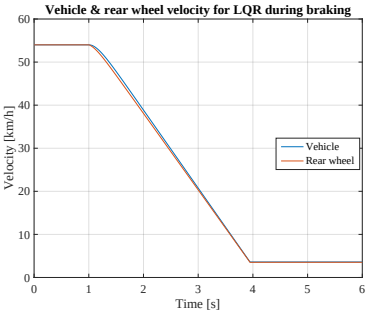

(b) **Test 2:** Vehicle & wheel velocity.

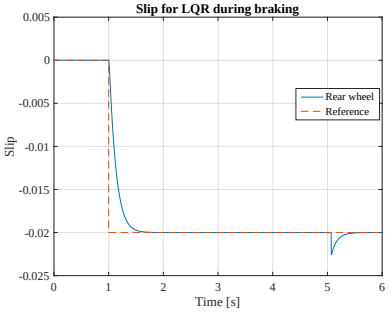

(c) **Test 1:** Slip.

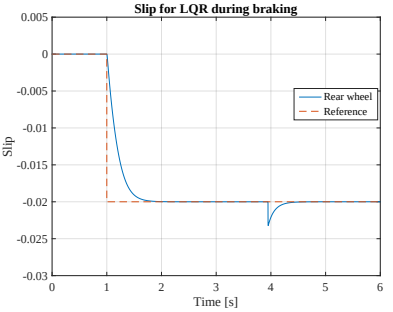

(d) **Test 2:** Slip

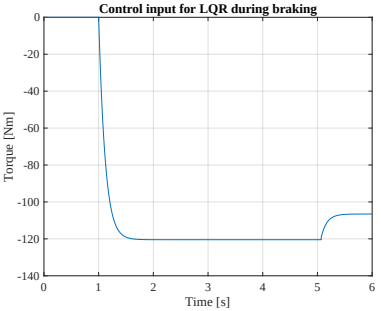

(e) **Test 1:** Control input.

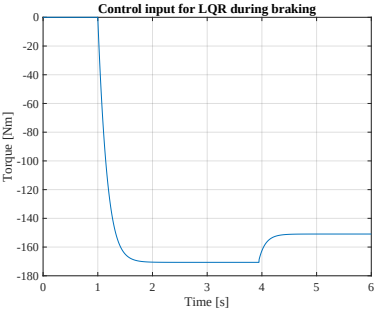

(f) **Test 2:** Control input.

Figure 6.11: Simulation with the LQR controller during braking for two different parameter sets for dry asphalt, Dry asphalt 1 (left) and Dry asphalt 2 (right). The controller is tuned for the parameter set Dry asphalt 1.

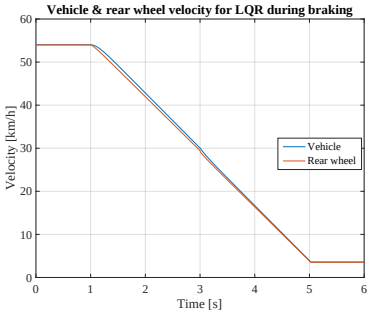

(a) **Test 3:** Vehicle & wheel velocity with a step disturbance on the control input.

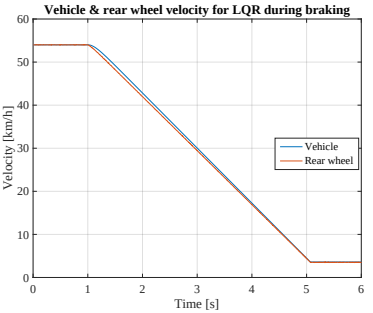

(b) **Test 4:** Vehicle & wheel velocity with noise added on the wheel velocity output.

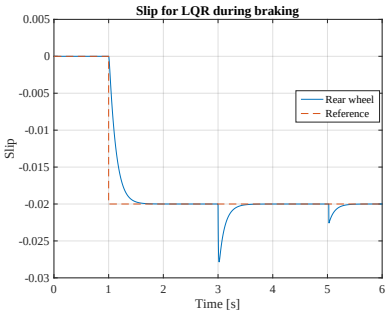

(c) **Test 3:** Slip with a step disturbance on the control input.

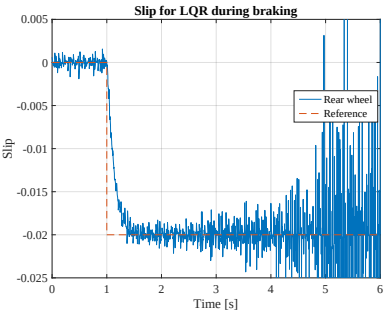

(d) **Test 4:** Slip with noise added on the wheel velocity output.

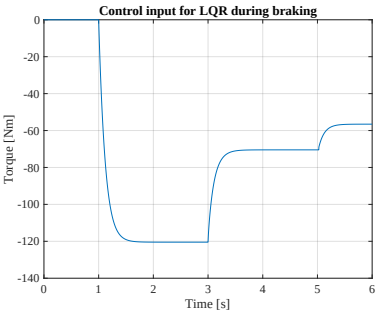

(e) **Test 3:** Control input with a step disturbance on the control input.

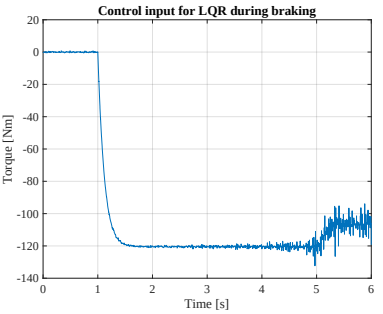

(f) **Test 4:** Control input with noise added on the wheel velocity output.

Figure 6.12: Simulation with the LQR controller during braking with a step disturbance of -50 Nm on the input (left) and white noise added on the rear wheel velocity with a variance of 0.001 (right).

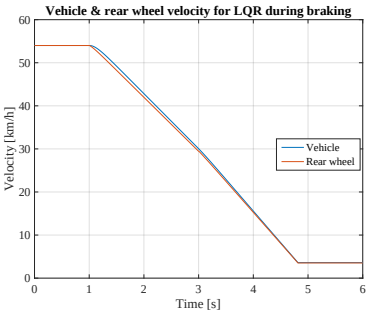

(a) **Test 5:** Vehicle & wheel velocity with changing road conditions.

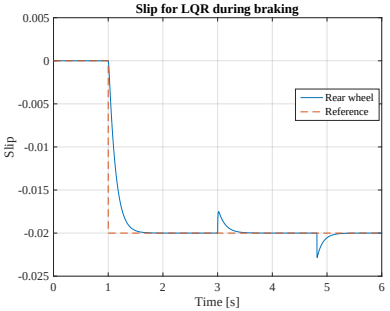

(b) **Test 5:** Slip with changing road conditions.

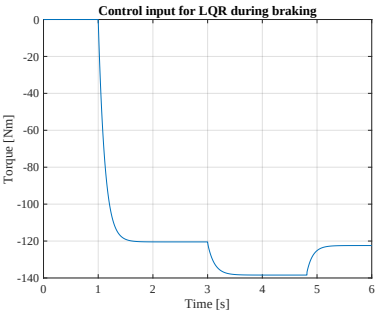

(c) **Test 5:** Control input with changing road conditions.

Figure 6.13: Simulation with the LQR controller during braking with changing road conditions from dry asphalt to wet asphalt at $t = 3$ seconds.

In Figure 6.16 the result of *Test 5* is shown. There is an initial transient in the slip after the road conditions are changed. The controller is responding fast on the changed road conditions by decreasing the applied torque.

Braking: Figure 6.17 shows the results of the MPC controller during braking with two different parameter sets for dry asphalt, i.e., *Test 1* and *Test 2*. The controller is able to decelerate faster for parameter set 2, which is due to the tire parameters themselves not the controller's performance.

Figure 6.18 shows two scenarios with different disturbances acting on the system. In Figures 6.18a, 6.18c and 6.18e the result of *Test 3* is shown. The controller's response is fast and counteracts the disturbance by increasing the driving torque.

Figures 6.18b, 6.18d and 6.18f show results of *Test 4*. The noise is very apparent in the slip for lower velocities and the signal is very noisy when the vehicle is almost at full stop. As in the acceleration case, the noise is clearly seen affecting the control input too.

In Figure 6.19c the result of *Test 5* is shown. There is an initial transient in the slip after the conditions are changed. The controller responds by increasing the applied torque. The peaks which appear in Figures 6.17c, 6.17d, 6.18c and 6.19b are due to the velocity approaching 0 km/h. The increase of noise at the end of the simulation after $t = 5$ seconds in Figure 6.18d is due to the velocity v approaching 0 km/h, the system is sensitive for noise at lower velocities. The negative estimation of the vehicle velocity in Figures 6.17a, 6.17b, 6.18a, 6.18b and 6.19a is also due to the velocity v approaching 0 km/h, whereas in a real–world implementation the estimation should be turned off for velocities near 0 km/h.

6.3 Comparison

In this section analysis and comparisons of the controllers will be made based on the simulations.

PID

The PI controller in the acceleration case performs well under normal circumstances with only some small overshoot for the second set of parameters, but still fully acceptable. With changing road conditions the controller performance is a bit worse. The slip starts to oscillate due to the changing conditions, but the controller manages to stabilize the slip within 3 seconds. In the braking case the performance is good for both parameter sets, where the controller is a bit slower in the settling time for the second parameter set, which seems fair since the controller is not tuned for that set. Under changing road conditions, the controller does not generate the same oscillatory behaviour as in the acceleration case.

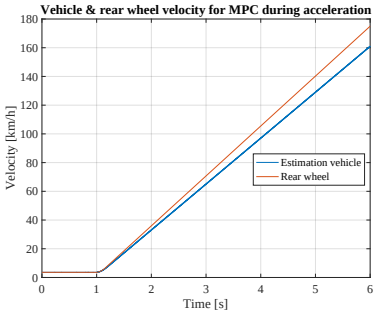

(a) **Test 1:** Vehicle & wheel velocity.

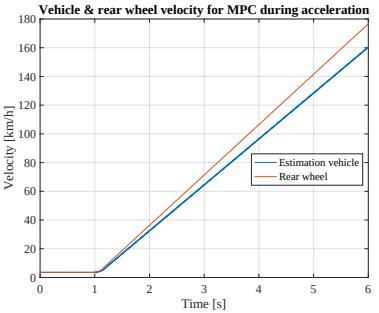

(b) **Test 2:** Vehicle & wheel velocity.

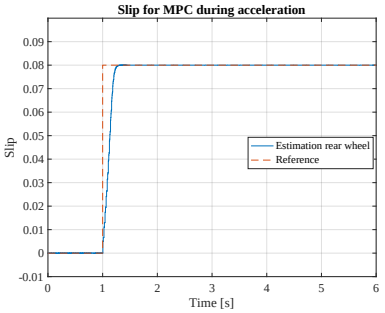

(c) **Test 1:** Slip.

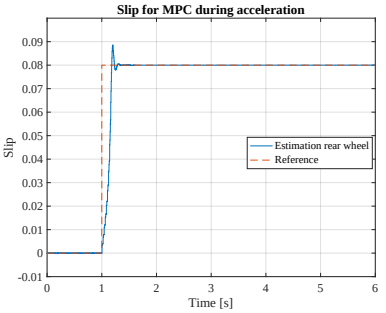

(d) **Test 2:** Slip

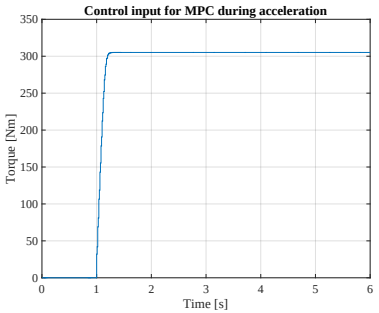

(e) **Test 1:** Control input.

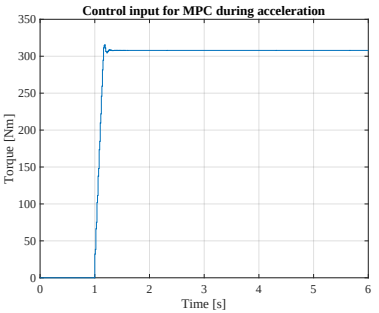

(f) **Test 2:** Control input.

Figure 6.14: Simulation with the MPC & EKF during acceleration for two different parameter sets for dry asphalt, Dry asphalt 1 (left) and Dry asphalt 2 (right). The controller is tuned for the parameter set Dry asphalt 1.

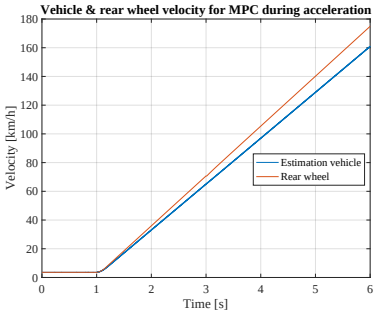

(a) **Test 3:** Vehicle & wheel velocity with a step disturbance on the control input.

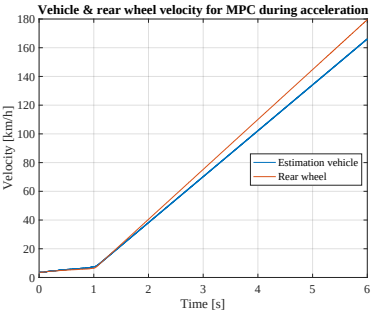

(b) **Test 4:** Vehicle & wheel velocity with noise added on the wheel velocity output.

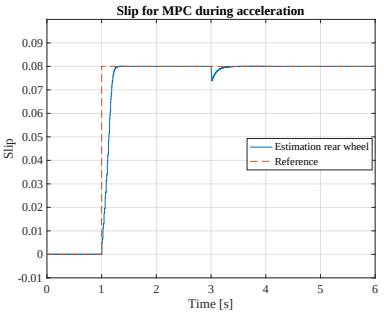

(c) **Test 3:** Slip with a step disturbance on the control input.

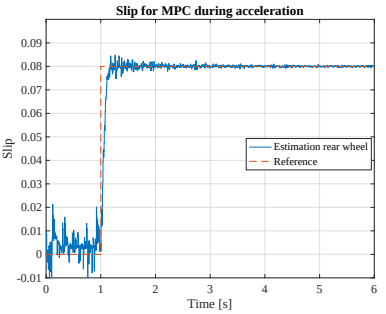

(d) **Test 4:** Slip with noise added on the wheel velocity output.

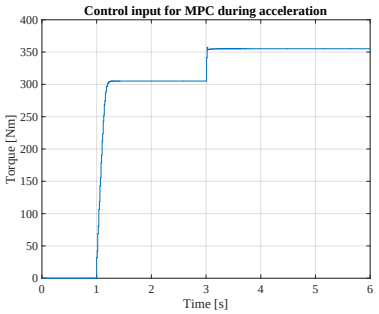

(e) **Test 3:** Control input with a step disturbance on the control input.

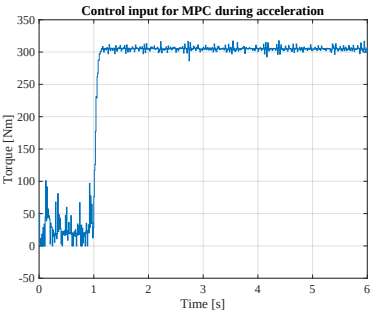

(f) **Test 4:** Control input with noise added on the wheel velocity output.

Figure 6.15: Simulation with the MPC & EKF during acceleration with a step disturbance of -50 Nm on the input (left) and white noise added on the rear wheel velocity with a variance of 0.001 (right).

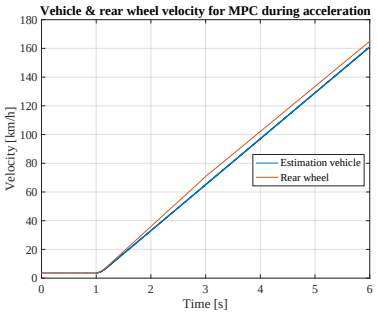

(a) **Test 5:** Vehicle & wheel velocity with changing road conditions.

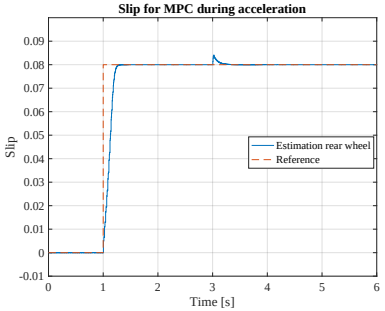

(b) **Test 5:** Slip with changing road conditions.

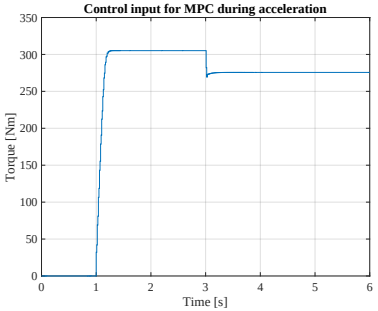

(c) **Test 5:** Control input with changing road conditions.

Figure 6.16: Simulation with MPC & EKF during acceleration with changing road conditions from dry asphalt to wet asphalt at $t = 3$ seconds.

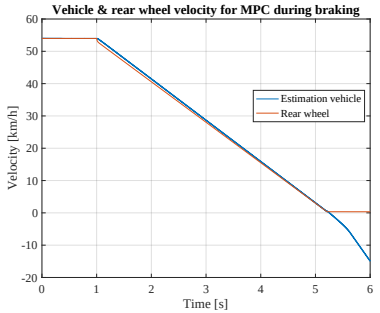

(a) **Test 1:** Vehicle & wheel velocity.

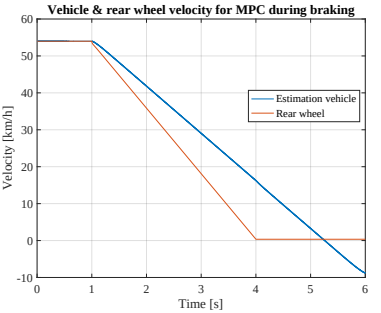

(b) **Test 2:** Vehicle & wheel velocity.

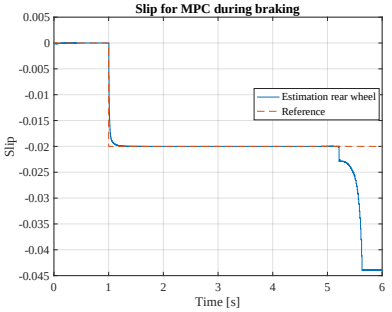

(c) **Test 1:** Slip.

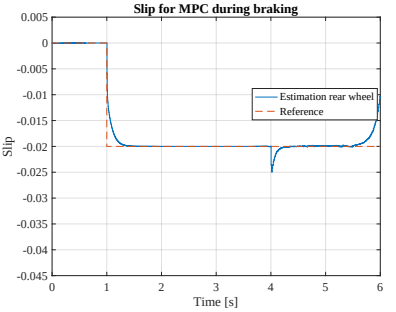

(d) **Test 2:** Slip

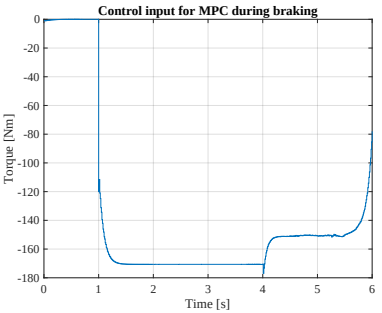

(e) **Test 1:** Control input.

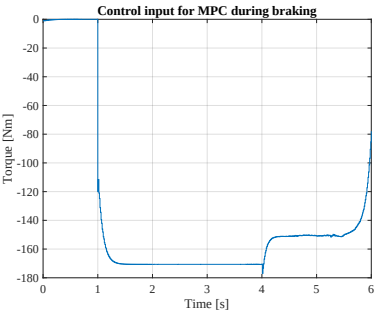

(f) **Test 2:** Control input.

Figure 6.17: Simulation with the MPC & EKF during braking for two different parameter sets for dry asphalt, Dry asphalt 1 (left) and Dry asphalt 2 (right). The controller is tuned for the parameter set Dry asphalt 1.

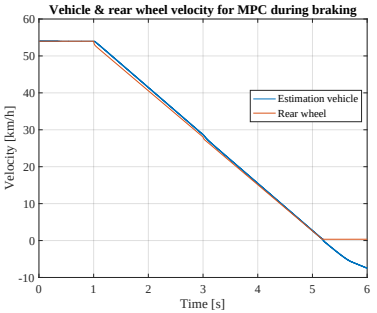

(a) **Test 3:** Vehicle & wheel velocity with a step disturbance on the control input.

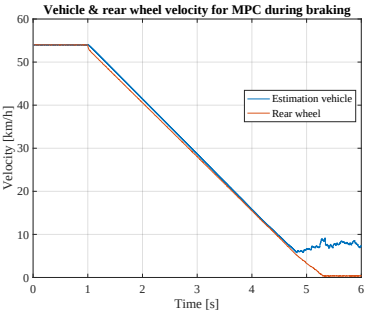

(b) **Test 4:** Vehicle & wheel velocity with noise added on the wheel velocity output.

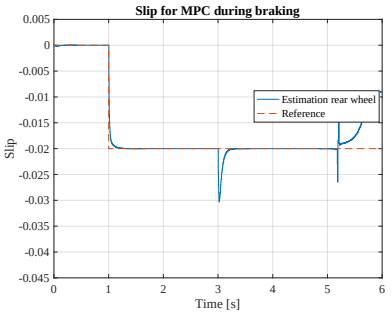

(c) **Test 3:** Slip with a step disturbance on the control input.

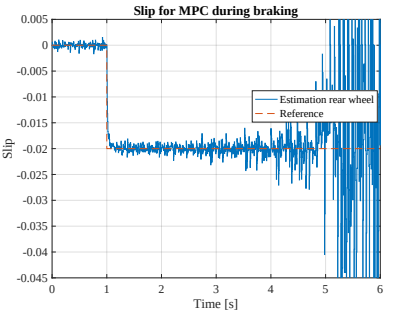

(d) **Test 4:** Slip with noise added on the wheel velocity output.

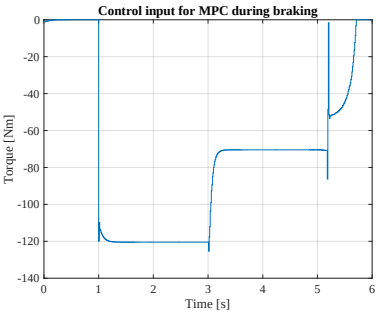

(e) **Test 3:** Control input with a step disturbance on the control input.

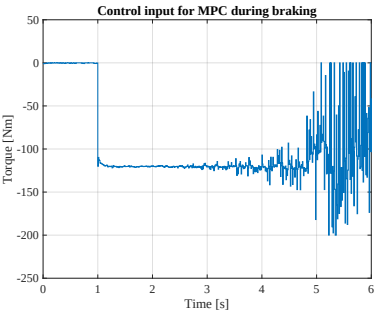

(f) **Test 4:** Control input with noise added on the wheel velocity output.

Figure 6.18: Simulation with the MPC & EKF during braking with a step disturbance of -50 Nm on the input (left) and white noise added on the rear wheel velocity with a variance of 0.001 (right).

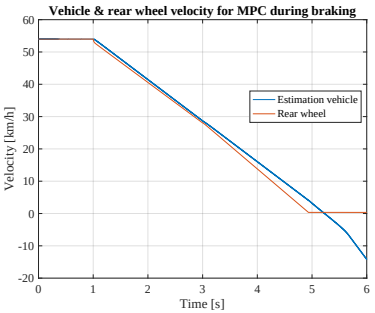

(a) **Test 5:** Vehicle & wheel velocity with changing road conditions.

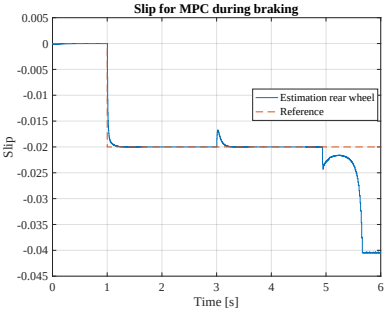

(b) **Test 5:** Slip with changing road conditions.

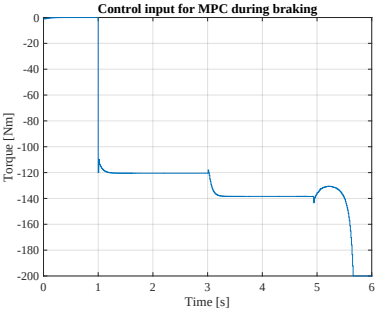

(c) **Test 5:** Control input with changing road conditions.

Figure 6.19: Simulation with MPC & EKF during braking with changing road conditions from dry asphalt to wet asphalt at $t = 3$ seconds.

LQR

The LQR controller performs well for both parameter sets during both acceleration and braking. The performance is very similar to the PI controller under these circumstances. The LQR controller performs better in the case when the road conditions are changing in the acceleration case, the slip does not start to oscillate as with the PI controller and the LQR controller manages to stabilize the slip around 0.5 seconds. In the braking case there is no difference between the LQR controller and PI controller under changing road conditions. Another possible advantage of the LQR over the PI controller is the tuning part as mentioned earlier. Since the states represent physical quantities, the tuning might be a bit more intuitive compared to the PI controller. The LQR controller seems to be more sensitive to noise than the PI controller, especially in the acceleration case since the noise appear more apparent on the control input. This is probably due the tuning of the controller.

MPC

The MPC performs well for both parameter sets on dry asphalt, both during acceleration and braking. It settles in shortest time of all three controllers. This might be due to more aggressive tuning, though. The controller seems to have some robustness against parameter uncertainty in the model. The MPC is a bit more sensitive to noise compared to the PI controller and the LQR controller. This is very apparent in the control input where the signal have more noise. This might be harmful for the electric motor to have this kind of varying signal and should be considered if implementation on a real vehicle is performed. The MPC is also handling the changing road conditions very well, even though this condition is not modelled.

7

Implementation

In this chapter the choice and implementation of the controller are discussed. A control logic for activation and de-activation is also discussed. Also a method to control acceleration and regenerative braking with only the accelerator pedal is presented. The controller, logic and the single-pedal control was implemented in C-code and tested on the vehicle in real–world experiments.

7.1 Control Strategy

From Chapter 6 all three controllers showed similar performance. Based on these results a gain–scheduled discrete PI controller in parallel form was implemented due to its simplicity and for being so well documented in literature and articles. The controller was discretized using the forward difference approximation. A sampling frequency of 100 Hz was used. In order to handle both the acceleration and braking case, two PI controllers are running in parallel with each other and tracking the currently applied input.

Anti-windup & Bumpless Transfer

A method for preventing the integral part of the controller to keep integrating the error when the actuator saturates is needed in order to prevent large transients. Otherwise the controller will keep integrating the error and the integrating part may grow very large. In order for the integral part to return to normal, the sign of the error will have to be opposite for a long period of time.

One way to cope with this problem is to add an extra feedback path to the integral part. This added feedback path is the difference between the actual sent (and possibly saturated) input to the actuator and the output from the controller. This difference is then scaled with a tracking gain $K_t = 1/T_t$, which determines the rate at which the integral part is modified to accommodate for actuator saturation [Åström and Wittenmark, 2011]. This will prevent the integral part to wind-up during saturation since the control signal and the saturated signal will differ. When no saturation occurs, the difference between the two signals will be zero.

Table 7.1: PI parameters for different velocities.

Gain scheduled PI - parameters		
Velocity km/h	**Acceleration**	**Braking**
$54 < v$	$K = 22.5$, $K_\mathrm{i} = 4018.0$	$K = 15.0$, $K_\mathrm{i} = 6255.0$
$54 \leq v < 83$	$K = 350.0$, $K_\mathrm{i} = 3977.0$	$K = 250.0$, $K_\mathrm{i} = 6937.5$
$83 \leq v < 108$	$K = 500.0$, $K_\mathrm{i} = 3787.86$	$K = 400.0$, $K_\mathrm{i} = 7280.0$

Another aspect that needs to be considered is to make sure that the state of the system is correct when switching between manual and automatic operation. Since the control signal may differ from the manual signal when operating in manual mode, the controller needs to be initialized correctly in order to prevent any jumps in the control signal when switching between the different modes occurs. The tracking method mentioned in the previous paragraph solves this problem too [Åström and Wittenmark, 2011].

Gain Scheduling

As seen in Figures 3.4 and 3.5, the bandwidth of the system decreases with increasing velocities. This could be compensated with gain scheduling by letting the velocity act as decision variable for when the operating conditions change and thus when the control parameters should be changed. The controller was tuned for four different velocities for both acceleration and braking. The chosen velocities were 1 m/s, 15 m/s, 23 m/s and 30 m/s. The scheduling part is implemented as a simple look-up table. The controller parameters can be seen in Table 7.1. Since no standardized parameters for the Pacejka model was found for surfaces such as gravel, the controller's tuning was based on the results from the simulation on dry asphalt, which then was scaled down iteratively. For the implementation the control parameter for the integral gain $1/T_\mathrm{i}$ was rewritten to K_i in order to avoid division in the calculations of the control output, since division is more demanding for the CPU compared to multiplication.

Changes between different parameters may cause large changes in the output. This can be prevented by simply implementing the integral state as:

$$I = x_\mathrm{i}(t) = \int_0^t \frac{K(s)}{T_\mathrm{i}(s)} e(s)ds = \int_0^t K_\mathrm{i} e(s)ds \tag{7.1}$$

instead of letting the integral part be defined as

$$I = \frac{K(s)}{T_\mathrm{i}(s)} x_\mathrm{i} = K_\mathrm{i} x_\mathrm{i} = K_\mathrm{i} \int_0^t e(s)ds \tag{7.2}$$

The discrete form of the integral part then becomes:

$$I_{k+1} = I_k + T_s \frac{K}{T_i} e_k = I_k + T_s K_i e_k \tag{7.3}$$

7.2 Control Logic

Some kind of control logic is necessary in order to switch between manual mode and automatic mode. This needs to be done in a safe way and the controller is never allowed to output a higher torque than the driver. The logic can be described by a finite state machine (FSM) and it is based on the method suggested in [Savaresi and Tanelli, 2010].

Slip control is a safety feature and it should only be activated when the slip λ exceeds a given threshold λ_{thr}. To prevent the controller to be activated due to noisy signals, a second conditions is added which states that the demanded input torque by the driver, T_{drv}, is greater than the controller input T_{ctr}. Then a third condition on the velocity is added to ensure closed-loop stability for lower speeds.

Figure 7.1 shows the FSM for the control logic. The activation condition for the acceleration case, A_{on}, is defined as:

$$(\lambda > \lambda_{thr}^{a}) \;\&\; (T_{drv} > T_{ctr}^{a}) \;\&\; (v > v_{thr}) \tag{7.4}$$

and the de-activation condition, A_{off}, is defined as

$$T_{drv} \leq T_{ctr} \tag{7.5}$$

The activation and de-activation conditions for the braking case are similar to the acceleration case but only reversed, where the activation condition, B_{on}, is

$$(\lambda < \lambda_{thr}^{b}) \;\&\; (T_{drv} < T_{ctr}^{b}) \;\&\; (v > v_{thr}) \tag{7.6}$$

and de-activation condition, B_{off}, is defined as

$$T_{drv} \leq T_{ctr} \tag{7.7}$$

7.3 Single Pedal Control

As discussed earlier, in electric vehicles or hybrid vehicles regenerative braking is commonly used to increase the range of the vehicle by letting the electric motor act as a generator during braking. In some electric vehicles with regenerative braking a single-pedal control system (SDP) is utilized [Liu et al., 2020]. When SDP is utilized the accelerator pedal is used for both acceleration and regenerative braking. The pedal travel is related to the applied torque, both with respect to its magnitude

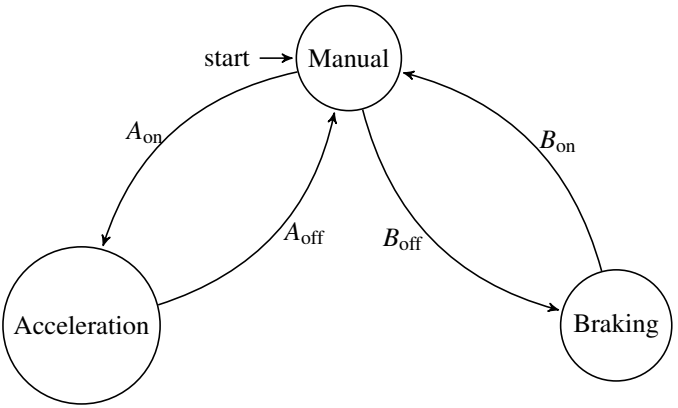

Figure 7.1: FSM of the control logic.

Table 7.2: Mapping for pedal travel with varying velocity.

	Velocity km/h							
Pedal travel %	v_1	v_2	v_3	v_4	v_5	v_6	v_7	v_8
p_1	C	R	R	R	R	R	R	R
p_2	A	C	R	R	R	R	R	R
p_3	A	A	C	R	R	R	R	R
p_4	A	A	A	C	R	R	R	R
p_5	A	A	A	A	C	R	R	R
p_6	A	A	A	A	A	C	R	R
p_7	A	A	A	A	A	A	C	C
p_8	A	A	A	A	A	A	A	C

and direction. By pressing on the pedal a positive torque will be applied as in a conventional accelerator pedal and the vehicle will start to accelerate and by releasing the pedal regenerative braking will used and a negative torque will be applied.

An SDP strategy presented in [Liu et al., 2020] was implemented. The method works as following, by defining three driving states, acceleration (A), coasting (C) and regenerative braking (R): Acceleration corresponds to 35%–100% of the pedal travel, coasting corresponds to 30%–35% of pedal travel and regenerative braking between 0%–30%. These ranges vary with the velocity, which can be seen in Table 7.2. A pedal travel $\geq$ 35% results in a linear increase in torque. In coasting, i.e., in the range of 30%–35%, it will result in zero torque and in the range of regenerative braking the braking torque is also applied linearly. A part of the mapping of pedal travel vs. velocity is shown in Table 7.2.

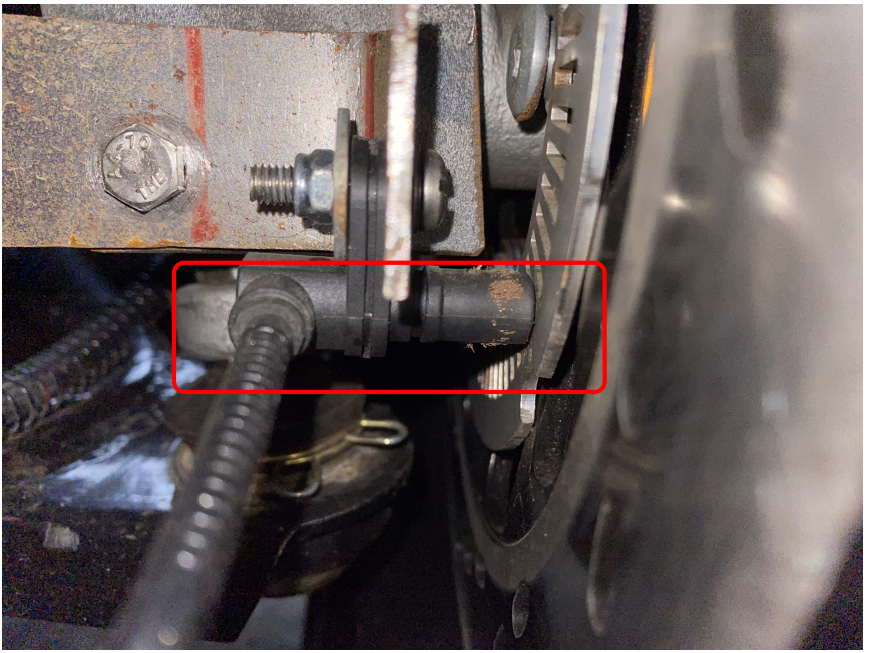

Figure 7.2: Placement of the ABS sensor for vehicle velocity measurement.

7.4 Sensor Integration

In order to obtain a good estimate of the slip, measurements of the vehicle's velocity and the velocity of the driven rear wheel are paramount. To get good measurements of the vehicle's velocity, the mounting and placement for the Hall sensors are crucial. The sensor must be mounted very close to the teethed encoder disc of the front wheel(s) and the gap should be only a few millimeters between the sensor and the encoder disc, see Figure 7.2. The sensor should also be centered to the disc. Two sensors were used, one on each front wheel. The velocity of the vehicle was then estimated by the average of these velocity measurements:

$$\bar{V}_{\mathrm{x}} = \frac{V_{\mathrm{R}} + V_{\mathrm{L}}}{2} \tag{7.8}$$

where V_{R}, V_{L} are the right front wheel and left front wheel velocity measurement, respectively. The velocity of the rear wheel is measured by the built in Hall sensors within the motor and was already implemented by Omotion AB themselves.

8

Experiments

In this chapter the results of real-world experiments of the controller discussed in Chapter 7 are presented and discussed, how they were performed and in what conditions they were performed in both acceleration and the regenerative braking case. A comparison between the two cases of when the controller is activated and deactivated is made and an analysis of the performance of the controllers is made.

8.1 Surface Conditions

The following tests in this section were performed on gravel and the controllers have been tuned for these conditions. This type of surface was chosen since it was easy to provoke undesirable slip during both acceleration and braking. Although the choice of surface makes the control problem harder since the surface is neither even nor homogeneous, which may cause variability in the slip, and should be considered as disturbances acting on the system.

Acceleration

The acceleration tests were performed along a straight line and with full throttle.

Controller turned off: Figure 8.1 shows experimental results during acceleration with the controller turned off. The test is performed driving along a straight line with an initial velocity of 0 km/h. The initial slip is very high and the vehicle becomes unstable. Corrections with the steering wheel is necessary in order to drive along a straight line and keep the vehicle under control. The overall driving experience feels unsafe under these circumstances.

Controller turned on: Figure 8.2 shows experimental results during acceleration with the controller turned on with two different slip references, $\lambda^* = 0.06$ and $\lambda^* = 0.04$. The tests are performed along a straight line with an initial velocity of 0 km/h. Note that the controller was not allowed to intervene for velocities below 3.6 km/h in these test cases.

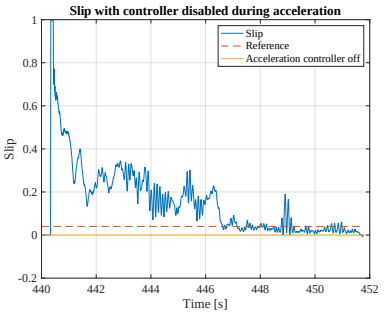

(a) Rear wheel slip.

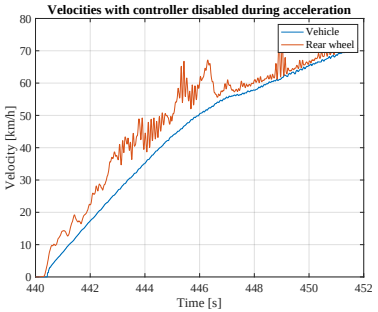

(b) Vehicle velocity & rear wheel velocity.

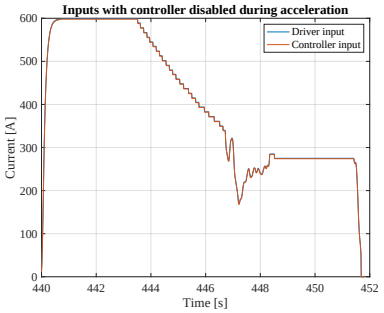

(c) Driver input & controller input.

Figure 8.1: Controller disabled during acceleration.

In Figures 8.2a, 8.2c and 8.2e the controller takes over at around $t = 23$ s, where the controller due to the high slip drastically lowers the input to the motor. In Figures 8.2b, 8.2d and 8.2f the controller takes over at around $t = 157$ s, where the controller due to the high slip drastically lowers the input to the motor. In this case it also takes approximately around a second for the controller to settle in around the reference. The variability in the slip is expected to be due to the inhomogeneous surface, although there seem to be some sort of oscillations in the measurements of wheel velocity, which also should have some impact on the performance of the controller.

In Figure 8.3 the activation condition is changed for the controller and it is now allowed to take over for velocities above 0 km/h. The controller is activated at around $t = 42$ s. It takes little more than a second for the controller to settle in around the reference. Changing the activation conditions does not seem to improve the transient response of the controller. The controller is activated a bit earlier though, compared to the first case.
The driving experience with the controller feels much safer and no corrections with the steering wheel is necessary in order to keep the vehicle under control.

In Figure 8.4 a comparison of the slip with controller turned off and on is shown. It is obvious that the controller is reducing the slip.

Braking

The braking tests were performed with only the regenerative braking of the electric motor, i.e., the hydraulics brakes were not used in the experiments since the ABS system was not fully implemented at the time of testing. In order to prevent the rear wheel from locking up due to the hydraulic brakes, these were not used.

Controller turned off: Figures 8.5a, 8.5c and 8.5e show experimental results during braking with the controller turned off. The test is performed by driving along a straight line with an initial velocity of 70 km/h. The initial slip is not as high in the braking case due the to difference in available torque during braking compared to acceleration.

Controller turned on: Figures 8.5b, 8.5d and 8.5f show experimental result during braking with the controller turned on. The test is performed by driving along a straight line with an initial velocity of 70 km/h. The controller takes over at around $t = 227$ s. The settling time for braking case is much more instant compared to the acceleration case. This is mainly due to much lower braking torque available during regenerative braking. The effect of the controller is not as obvious as in the acceleration case. The same oscillations are present in the measurements of wheel velocity and the slip as observed in the acceleration case.

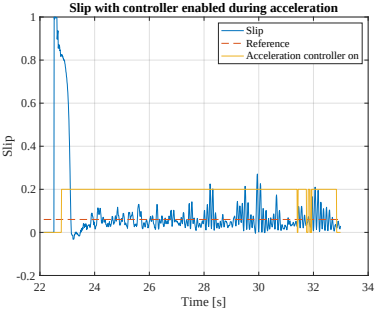

(a) Rear wheel slip, $\lambda^* = 0.06$.

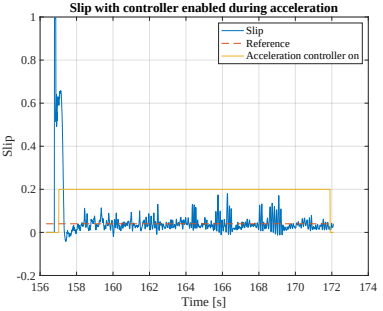

(b) Rear wheel slip, $\lambda^* = 0.04$.

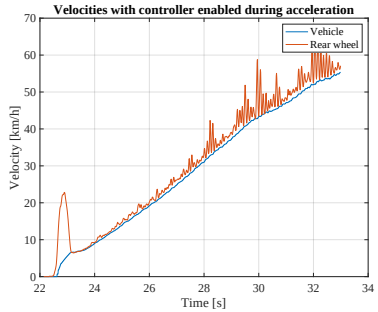

(c) Vehicle velocity & wheel velocity.

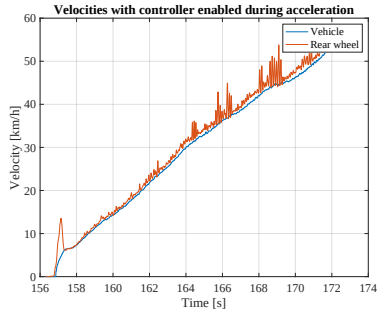

(d) Vehicle velocity & wheel velocity.

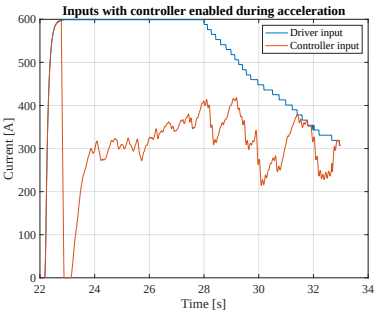

(e) Driver input & controller input.

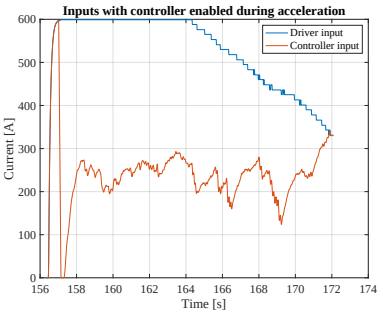

(f) Driver input & controller input.

Figure 8.2: Controller enabled during acceleration with different slip references.

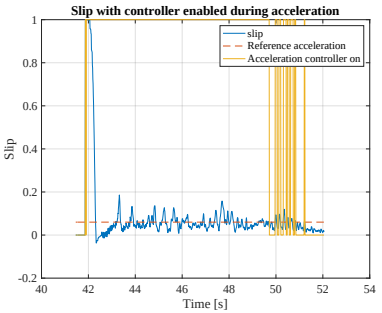

(a) Rear wheel slip, $\lambda^* = 0.06$.

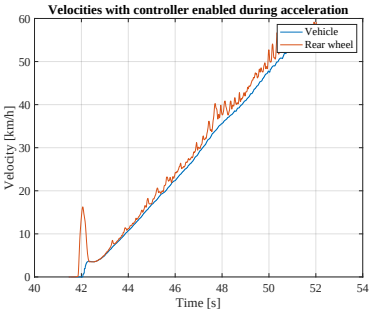

(b) Vehicle velocity & wheel velocity.

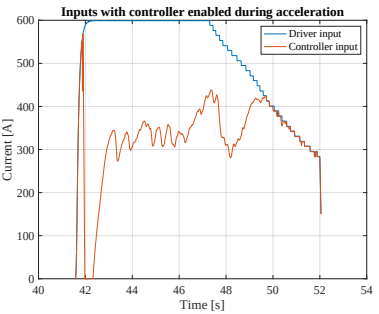

(c) Driver input & controller input.

Figure 8.3: Controller enabled during acceleration with changed activation conditions, i.e., allowed to intervene for velocities ≥ 0 km/h.

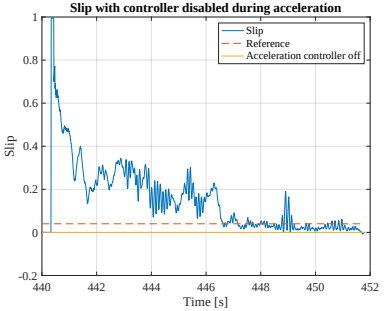

(a) Rear wheel slip with the controller turned off.

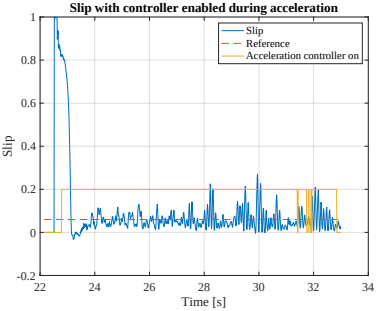

(b) Rear wheel slip with the controller on, $\lambda^* = 0.06$.

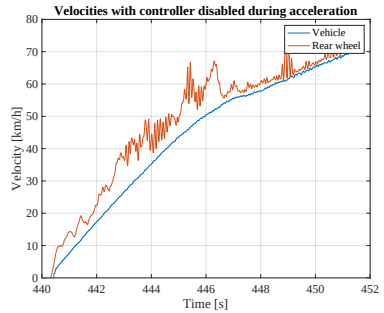

(c) Vehicle & wheel velocity with the controller off.

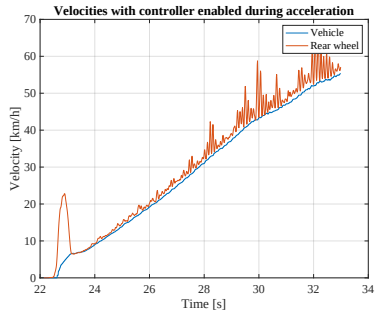

(d) Vehicle & wheel velocity with the controller on.

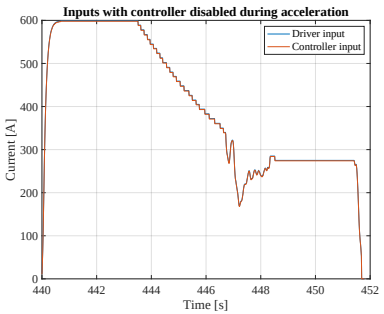

(e) Driver input with the controller off.

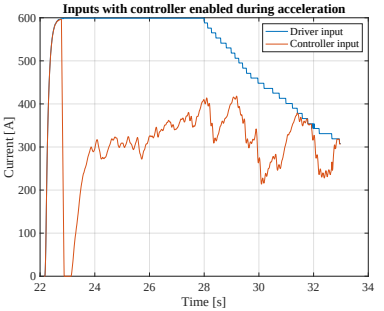

(f) Driver & controller input with the controller on.

Figure 8.4: Comparison between experiments with the controller disabled and enabled during acceleration.

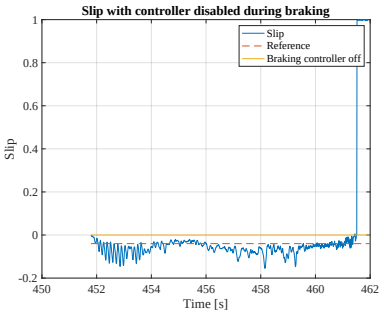

(a) Controller off: Rear wheel slip.

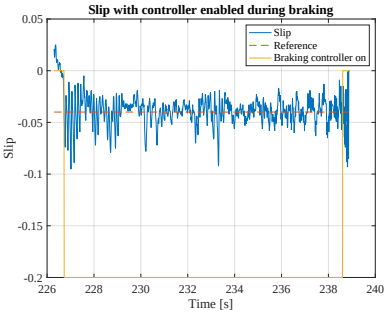

(b) Controller on: Rear wheel slip, $\lambda^* = -0.04$.

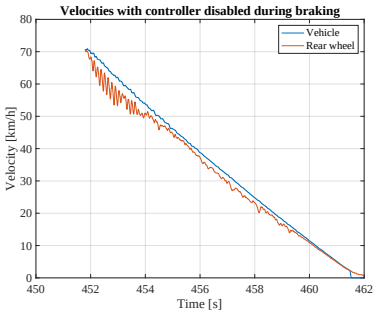

(c) Controller off: Vehicle velocity & wheel velocity.

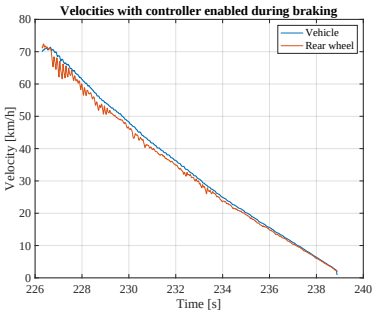

(d) Controller on: Vehicle velocity & wheel velocity.

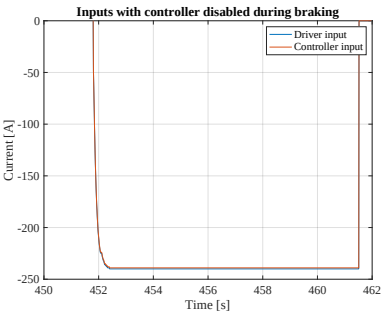

(e) Controller off: Driver input & controller input.

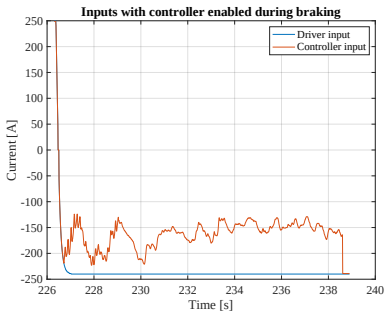

(f) Controller on: Driver input & controller input.

Figure 8.5: Comparison between experiments with the controller disabled and enabled during braking.

8.2 Spectrum Analysis

In the previous section it was mentioned that some of the signals seem to contain oscillating behaviour. In Figure 8.1 it is shown very clearly in the measurement of the rear wheel velocity. The same oscillations are seen in Figure 8.2, e.g., where the controller is turned on. It also seems to get worse with higher velocities.

Controller turned off: In Figure 8.6 periodograms of the signals when the controller is turned off for both acceleration and braking are shown. It is very clear that there is some content in the signals between 5–10 Hz when looking at the rear wheel measurement in Figure 8.6c during acceleration. This is also naturally then seen in the slip signal, see Figure 8.6a. By looking at the rear wheel measurements during braking in Figure 8.6d there is also some content in the same frequency range, although a bit more damped.

Controller turned on: In Figure 8.7 the periodograms for the case when the controller is turned on during acceleration and braking are shown. The same content as in the case when the controller is turned off can be seen in the velocity signals and the control signal, i.e., in the range of 5–10 Hz. Also the same behaviour between the acceleration and braking is shown. Since the same signal content is seen in both cases for when the controller is turned off and on, is seems that it is not the controller that contributes to this signal.

8.3 Analysis

As we saw in the comparisons in Figures 8.4 and 8.5, it is obvious that the controllers try to regulate the slip. The performance of the controllers is satisfactory in the sense that they try to settle in around the references and that safety and comfort are increased with a controller. However, more testing and tuning of the control parameters is needed in order to get even better results, especially for the higher velocities.

As mentioned in the beginning of the chapter, no hydraulic brakes were used in the braking test since the ABS system was not fully implemented at the time of the experiments. So no conclusion can be drawn for the braking controller's performance when there is disturbances in the form of hydraulic braking acting on the rear wheel. This type of scenario is probably also a typical situation where the braking controller will make the most difference.

The source of the oscillations in the measurement of the wheel velocity is not known, but it might be due to the surface inregularities or some disturbance signal coming from the motor/ inverter or just some settings in the software for the inverter. It may also be due to some sort of aliasing effect.

Something worth mentioning as well is that with the current implementation of the controllers, regarding the implementation of the anti-windup and the bumpless

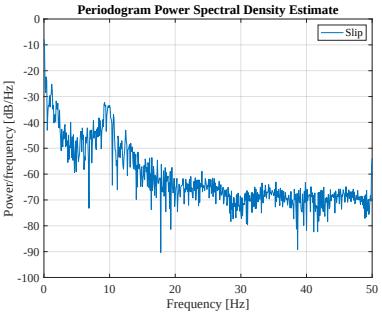

(a) Rear wheel slip during acceleration.

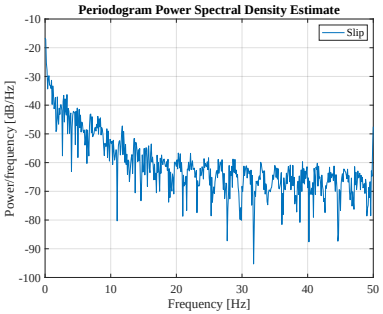

(b) Rear wheel slip during braking.

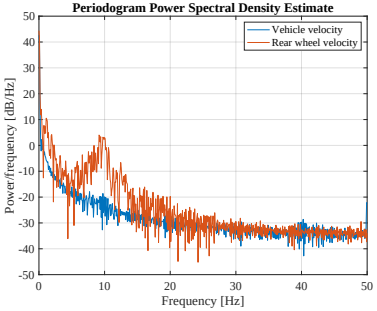

(c) Vehicle velocity & wheel velocity during acceleration.

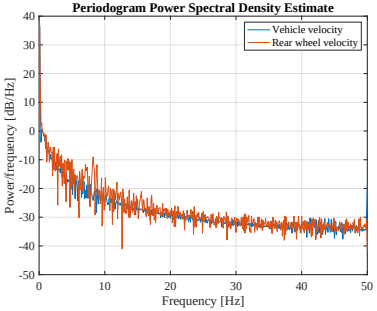

(d) Vehicle velocity & wheel velocity during braking.

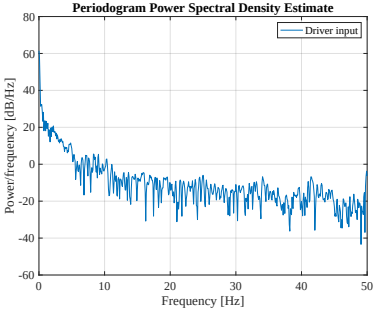

(e) Driver input & controller input during acceleration.

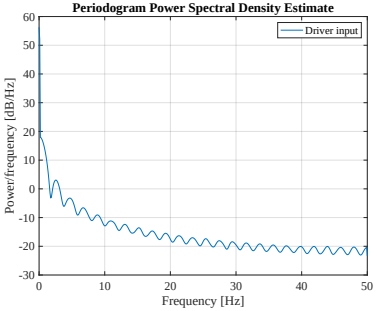

(f) Driver input & controller input during braking.

Figure 8.6: Periodograms of the signals with the controller disabled during acceleration and braking.

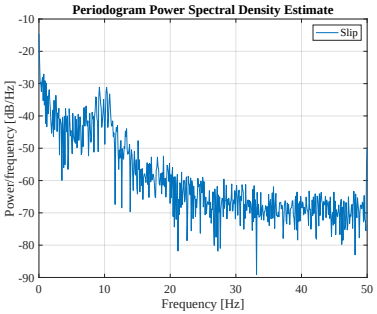

(a) Rear wheel slip during acceleration from Figure 8.2a.

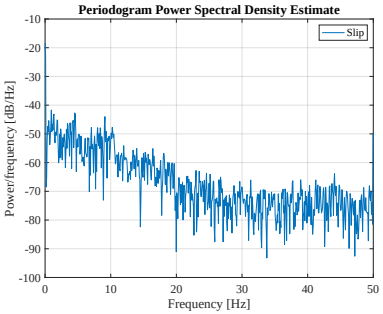

(b) Rear wheel slip during braking from Figure 8.5b.

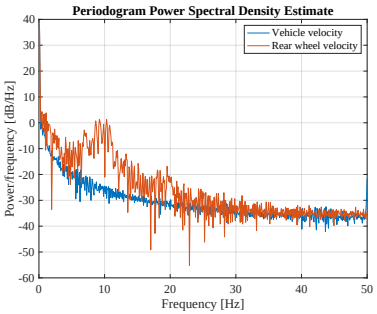

(c) Vehicle velocity & wheel velocity during acceleration from Figure 8.2c.

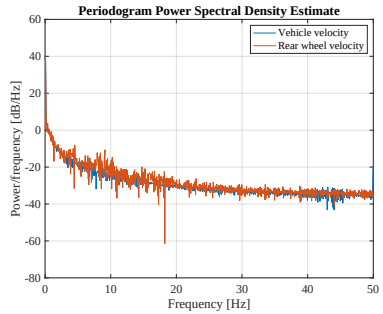

(d) Vehicle velocity & wheel velocity during braking from Figure 8.5d.

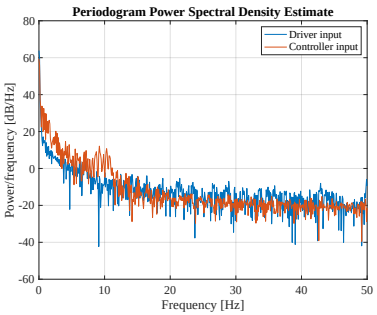

(e) Driver input during acceleration from Figure 8.2e.

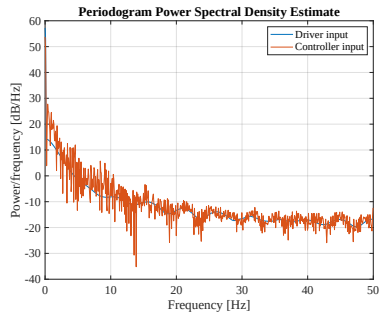

(f) Driver input during braking from Figure 8.5f.

Figure 8.7: Periodograms of the signals with the controller enabled during acceleration and braking.

transfer, is that the tuning range of the tracking constant is very small. No solution of this during the work was found. A consequence of this is that the rate at which the controller output is reset will be very limited which may limit the performance of the controller if a faster tracking is desired.

9

Discussion

In this chapter a discussion of the results and the analysis from the previous chapter is presented. The aim of this thesis was to design, implement and test a controller in order to control the slip of an electric three-wheeled vehicle. Another aspect of the thesis has been to compare different control structures in simulations.

This thesis aimed to answer a couple of questions. What type of controller is suitable to control the slip and how accurate model of the vehicle and the tire forces are required? Is it possible to use the same type of controller during regenerative braking and preventing the wheel lock-up? Is it possible to extend the range of the vehicle by incorporating regenerative braking and wheel the acceleration be improved with slip control? Finally, is it possible to improve the estimation of the longitudinal velocity of the vehicle?

A PI controller was designed, implemented and tested successfully. A PI controller was used for the acceleration and braking phase. Due to lack of time no experiments or analysis regarding if the regenerative braking would increase the range of the vehicle was performed. However, the range would most likely be increased, but a more interesting question would be to find out if the slip controller could be used to optimize the energy recovery with respect to braking force. No experiments to answer if the acceleration would be improved were done since the experiments were performed at gravel. The focus was instead switched to improve safety and drive ability since the surface was so slippery. Due to lack of time no investigation was done to see if the estimation of the velocity could be improved with an accelerometer.

9.1 Modelling

In this thesis, the dynamics of the slip and the tire force acting on the driving wheel were modelled. A nonlinear model of the tire forces in the form of Pacejka's Magic Formula was used whose parameters have been determined through empirical trials in previous research. The parameters used in this thesis were based on standardized values from sources, i.e., the tire parameters used may not correspond to the actual

tires used on the vehicle. An accurate model of tire forces is paramount in order to get a good starting point of the tuning of the controllers.

It should also be noted that the weight distribution on the rear wheel has a great impact on the dynamics of the tire. In the simulations an approximation was made regarding the weight, where it was assumed that the weight on the rear wheel was a third of the total weight of the vehicle. Later on during the work it was shown that it was approximately half of the total weight of vehicle that acted on the rear wheel. This should be taken into account for future tunings of the controllers, since the normal force F_z is directly related to the tire forces.

In this thesis all dynamics and control systems for the actuators of the vehicle were omitted, i.e., the dynamics of the electric motor and its components were not included, and the same goes for the hydraulic brakes. Including the dynamics of the electric motor should give a more accurate model of the vehicle and in turn also better control performance. By including the dynamics of the hydraulic brakes, or at least the amount of applied braking torque, could be used in the future to model some possible input disturbances to the vehicle.

9.2 Simulations

Simulations of three different controllers were made, namely PI, LQR and MPC. All three controllers were tested in different driving conditions and with different disturbances acting on the system. All controllers showed good performance in driving conditions with no disturbances, where the MPC had the fastest settling time. All three also showed good robustness against some degree of parameter uncertainty in the tire model. The controllers also performed well when a braking torque was added as an input disturbance, although when noise was added to the measurement of the rear wheel velocity, it is clear that all three controllers were sensitive to noise for lower velocities. The PI controller seems to handle the noise a little better than the other two, since noise is not as present on the control input. During tests with changing road conditions, the PI controller was much more sensitive for this kind of disturbance compared to the LQR and the MPC, at least in the acceleration. This might simply be due to high integral gain. Although the controllers perform a bit differently in various tests, they all show some promising results and they should be suitable for controlling the slip. In the future more tests at different velocities and other driving conditions should be performed in order to verify robustness and performance over a wider range of use cases.

9.3 Implementation

Two gain-scheduled PI controllers were implemented, one for the acceleration phase and one for the braking phase. Four different parameter sets for four different velocities were used. Experiments for all four velocities were never carried

out due to lack of time. In the future, more parameter sets for different velocities should be used in order to get tailored performance for a wider operating range, or at least velocity points should be a bit closer especially for lower velocities where slip dynamics is faster compared to for higher velocities. There is still some work regarding the tracking constant for the anti-windup/ bumpless transfer since the tuning range is currently very small. It is suspected that this has something to do with how the control signals is saturated in the control logic.

A Control logic for safe switching between manual and automatic mode was also developed. It is important that the controller never outputs a higher torque than the driver in order to ensure safety. A single-pedal control, SDP, was also implemented in order to control the driving and the braking torque of the electric motor with only the accelerator pedal. The implementation of the SDP was successful and was working as intended.

9.4 Experiments

Through real-world experiments, the PI controller's and the auxiliary system's performance and functionality were tested. The performance is satisfactory to the degree that it increases driveability and safety on low-friction surfaces such as gravel, although more testing and tuning is needed in order to get even better results. Tests in a wider range of velocities should be performed in the future in order to test the gain scheduling properly. Tests where the ABS system is activated should be performed in order to test the controller's performance when input disturbances of hydraulic brakes are applied. As already mentioned in Chapter 8, the source of the 5–10 Hz signal that appears on the measurement of the rear wheel velocity is not known and needs to be further studied in order to find out what is causing it.

10

Conclusion

The simulations of the PI, LQR and MPC controllers in both acceleration and braking show promising results for controlling the slip of a three wheeled electric motorcycle. The MPC were the best performing controller in the majority of the tests. Two PI controllers were implemented on the vehicle one for the acceleration case and one for the regenerative braking case, the performance of the controllers were tested in different experiments. The PI controllers were sufficient to ensure a safer driving experience on slippery surfaces such as gravel for both acceleration and regenerative braking. More testing in different driving conditions is needed to see how the controllers are performing in other use cases.

10.1 Future Work

Here, a summary of what kind of work is needed and can be done in the future in order to improve the performance is given.

For modelling some kind of parameter identification for the tire parameters should be made in order to get a more accurate estimation of the tire forces. The dynamics of the electric motor could also be included in order to improve the accuracy of the model.

With a better model of the system, the simulations should be more accurate. Simulations over a wider range of velocities should be made to ensure controller performance and robustness.

Implementation wise, a solution to the short tuning range of the tracking constant is needed. Alternatively, choosing another anti-windup method can be considered. It is also believed that with a faster sampling frequency, improved results could be obtained since the time constant is very fast at least for lower velocities. More real-world experiments of different velocities and on different types of surfaces are needed to be performed. With better models, more work could be done in the simulations regarding the tuning part of the controllers.

A

Model Appendix

A.1 Linearized Models

First-order Models

The linearization of the first-order models which were used for the design of the PI and LQR controllers in the acceleration case and braking case:

Acceleration

$$\begin{aligned} \boldsymbol{A}_{\mathrm{a}} = & -\frac{1}{V_{\mathrm{x}}}\left(-\frac{1}{m}-\frac{r^2}{J}2(1-\lambda_0)\right)F_{\mathrm{x}}(\lambda_0) \\ & -\frac{1}{V_{\mathrm{x}}}\left(\frac{1-\lambda_0}{m}+\frac{r^2}{J}(1-\lambda_0)^2\right)\frac{\partial F_{\mathrm{x}}}{\partial \lambda}(\lambda_0) \end{aligned} \tag{A.1}$$

and

$$\boldsymbol{B}_{\mathrm{a}} = \frac{(1-\lambda_0)^2}{J_{\mathrm{w}}V_{\mathrm{x}}}\, r \tag{A.2}$$

Braking

$$\boldsymbol{A}_{\mathrm{b}} = -\frac{1}{V_{\mathrm{x}}}\left[\left(\frac{1+\lambda_0}{m}+\frac{r^2}{J_{\mathrm{w}}}\right)\frac{\partial F_{\mathrm{x}}}{\partial \lambda}(\lambda_0)+\frac{F_{\mathrm{x}}}{m}(\lambda_0)\right] \tag{A.3}$$

and

$$\boldsymbol{B}_{\mathrm{b}} = \frac{r}{J_{\mathrm{w}}V_{\mathrm{x}}} \tag{A.4}$$

where

$$\begin{aligned} \frac{\partial F_{\mathrm{x}}}{\partial \lambda} \quad = \quad & [C\cdot D\cdot g\cdot m\cdot\cos(C\cdot\arctan(B\cdot X+E\cdot(\arctan(B\cdot X)-B\cdot X))) \\ & \cdot(B-E\cdot(B-B/(B^2\cdot X^2+1)))] \\ & /\,[(B\cdot X+E\cdot(\arctan(B\cdot X)-B\cdot X))^2+1] \end{aligned}$$

and

$$X = \lambda - s_{\mathrm{h}} \tag{A.5}$$

Second-order Models

For the design of the MPC, the second order nonlinear model were linearized and the following linear models were obtained for the acceleration case and the braking case respecively:

$$\dot{\boldsymbol{x}} = \boldsymbol{A}\boldsymbol{x} + \boldsymbol{B}\boldsymbol{u} \tag{A.6}$$

Acceleration

$$\boldsymbol{A}_{\mathrm{a}} = \begin{bmatrix} 0 & a_{12} \\ a_{21} & a_{22} \end{bmatrix} \tag{A.7}$$

where

$$\begin{aligned} a_{12} \;=\; & [C \cdot D \cdot g \cdot m \cdot \cos(C \cdot \arctan(B \cdot X + E \cdot (\arctan(B \cdot X) - B \cdot X))) \\ & \cdot (B - E \cdot (B - B/(B^2 \cdot X^2 + 1)))] \\ & / \left[(B \cdot X + E \cdot (\arctan(B \cdot X) - B \cdot X))^2 + 1\right] \end{aligned}$$

$$\begin{aligned} a_{21} \;=\; & [(r \cdot (T_b - T_m) \cdot (\lambda - 1)^2)/(J \cdot v^2)] \\ & - [(s_v + D \cdot g \cdot m \cdot \sin(C \cdot \arctan(B \cdot X + E \cdot (\arctan(B \cdot X) - B \cdot X))))) \\ & \cdot ((\lambda - 1)/m - (r^2 \cdot (\lambda - 1)^2)/J)]/v^2 \end{aligned}$$

$$\begin{aligned} a_{22} \;=\; & [(1/m - (r^2 \cdot (2 \cdot \lambda - 2))/J) \cdot (s_v + D \cdot g \cdot m \cdot \sin(C \cdot \arctan(B \cdot X \\ & + E \cdot (\arctan(B \cdot X) - B \cdot X))))]/v - [(r \cdot (2 \cdot \lambda - 2) \cdot (Tb - Tm))/(J \cdot v)] \\ & + [C \cdot D \cdot g \cdot m \cdot \cos[C \cdot \arctan(B \cdot X + E \cdot (\arctan(B \cdot X) - B \cdot X))] \\ & \cdot [B - E \cdot (B - B/(B^2 \cdot X^2 + 1))] \cdot ((\lambda - 1)/m - (r^2 \cdot (\lambda - 1)^2)/J)] \\ & / \left[(v \cdot ((B * X + E \cdot (\arctan(B \cdot X) - B \cdot X))^2 + 1))\right] \end{aligned}$$

and

$$X = \lambda - s_{\mathrm{h}} \tag{A.8}$$

$$\boldsymbol{B}_{\mathrm{a}} = \begin{bmatrix} 0 \\ (r \cdot (\lambda - 1)^2)/(J \cdot v) \end{bmatrix} \tag{A.9}$$

Braking

$$\boldsymbol{A}_{\mathrm{b}} = \begin{bmatrix} 0 & a_{12} \\ a_{21} & a_{22} \end{bmatrix} \tag{A.10}$$

where

$$\begin{aligned} a_{12} &= [C \cdot D \cdot g \cdot m \cdot \cos(C \cdot \arctan(B \cdot X + E \cdot (\arctan(B \cdot X) - B \cdot X))) \\ &\quad \cdot (B - E \cdot (B - B/(B^2 \cdot X^2 + 1)))] \\ &\quad / \left[(B \cdot X + E \cdot (\arctan(B \cdot X) - B \cdot X))^2 + 1\right] \end{aligned}$$

$$\begin{aligned} a_{21} &= [(r \cdot (T_b - T_m))/(J \cdot v^2)] \\ &\quad + [g \cdot m \cdot (r^2/J + (\lambda + 1)/m) \\ &\quad \cdot (s_v + D \cdot sin(C \cdot \arctan(B \cdot X + E \cdot (\arctan(B \cdot X) - B * X))))]/v^2 \end{aligned}$$

$$\begin{aligned} a_{22} &= -[(g \cdot (s_v + D \cdot \sin(C \cdot \arctan(B \cdot X + E \cdot (\arctan(B \cdot X) - B \cdot X)))))/v] \\ &\quad - [(C \cdot D \cdot g \cdot m \cdot \cos(C \cdot \arctan(B \cdot X + E \cdot (\arctan(B \cdot X) - B \cdot X))) \\ &\quad \cdot (r^2/J + (\lambda + 1)/m) \cdot (B - E \cdot (B - B/(B^2 \cdot X^2 + 1))))] \\ &\quad / \left[v \cdot ((B \cdot X + E \cdot (\arctan(B \cdot X) - B \cdot X))^2 + 1)\right] \end{aligned}$$

$$\boldsymbol{B}_{\mathrm{b}} = \begin{bmatrix} 0 \\ r/(J \cdot v) \end{bmatrix} \tag{A.11}$$

and

$$X = \lambda - s_{\mathrm{h}} \tag{A.12}$$

B

Experiment Appendix

In this chapter some results from different experiments with different velocities are presented. It should be noted that in the experiments presented here, the battery had not been charged for some time, which means that full power was not available during the experiments. This would only affect the acceleration phase though, in the regard that undesired slip is more difficult to provoke.

Acceleration

Figure B.1 shows experimental results during acceleration with an initial velocity of 7 km/h. The controller is activated around $t = 182$ s. Figure B.2 shows experimental results during acceleration with an initial velocity of 30 km/h and 50 km/h. In Figure B.2a the controller is activated around $t = 382.5$ s and then it switches on and off for a while. In Figure B.2b the controller is activated around $t = 427$ s and then it switches on and off for a while.

Braking

Figure B.3 shows experimental results during braking with an initial velocity of 30 km/h and 50 km/h. In Figure B.3a the controller is activated around $t = 285$ s. In Figure B.3b the controller is activated around $t = 92$ s.

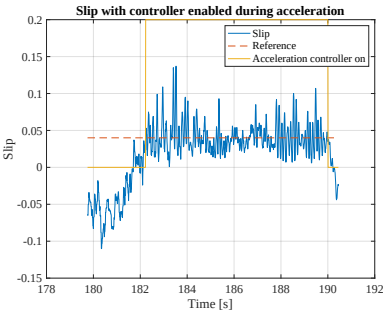

(a) Rear wheel slip.

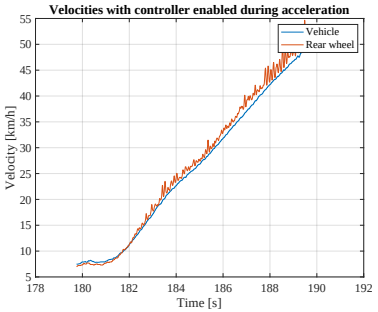

(b) Vehicle velocity & wheel velocity.

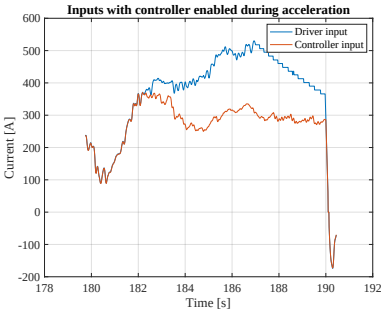

(c) Driver input & controller input.

Figure B.1: Controller enabled during acceleration with an initial velocity of 7 km/h.

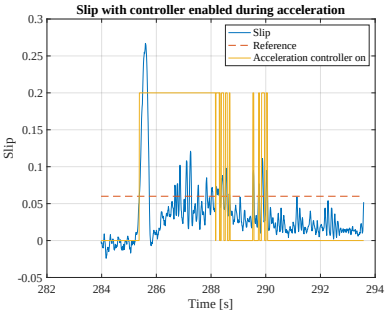

(a) Rear wheel slip during acceleration.

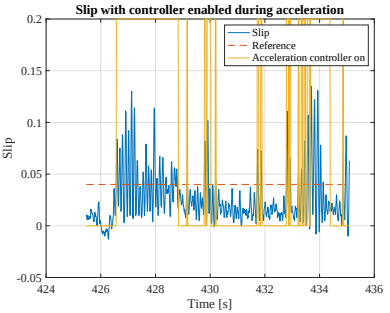

(b) Rear wheel slip during acceleration.

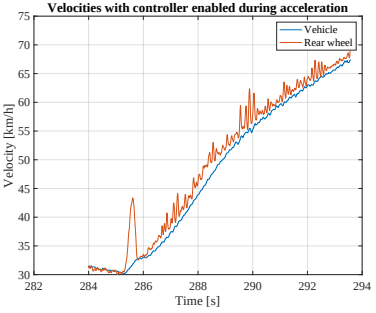

(c) Vehicle velocity & wheel velocity during acceleration.

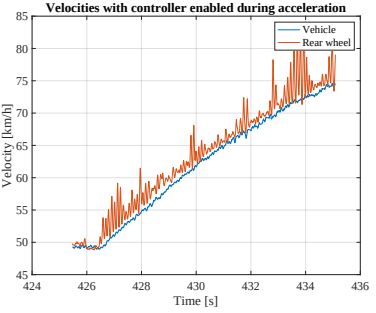

(d) Vehicle velocity & wheel velocity during acceleration.

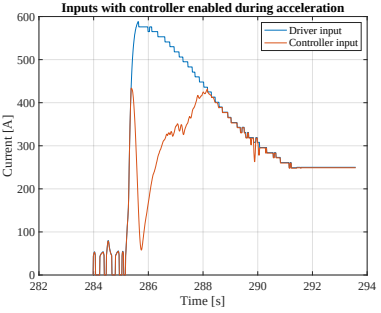

(e) Driver input during acceleration.

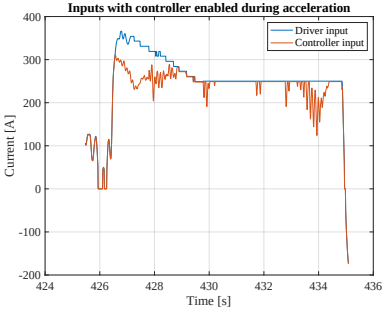

(f) Driver input during acceleration.

Figure B.2: Controller enabled during acceleration with an initial velocity of 30 km/h (left) and 50 km/h (right).

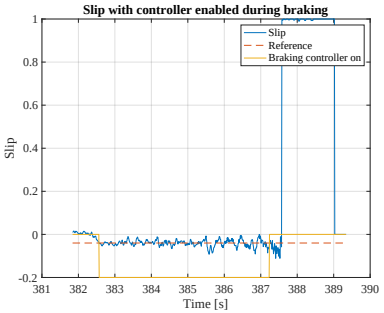

(a) Rear wheel slip during braking.

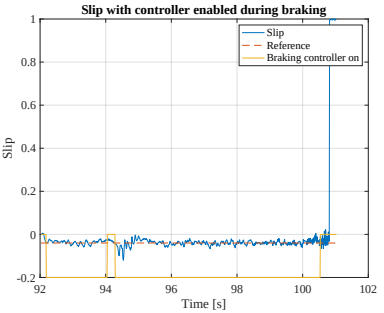

(b) Rear wheel slip during braking.

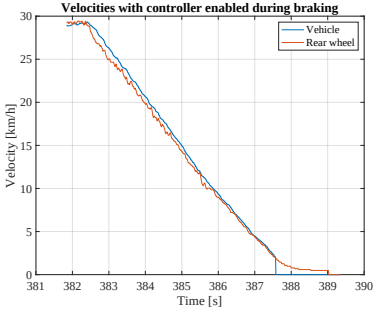

(c) Vehicle velocity & wheel velocity during braking.

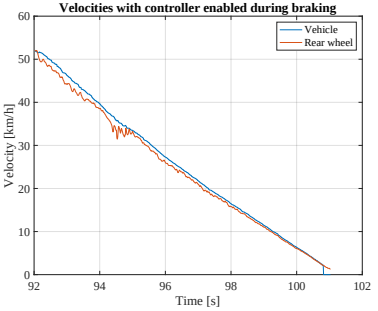

(d) Vehicle velocity & wheel velocity during braking.

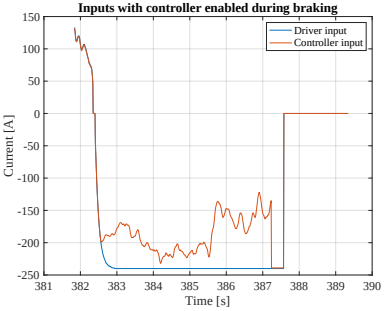

(e) Driver input during braking.

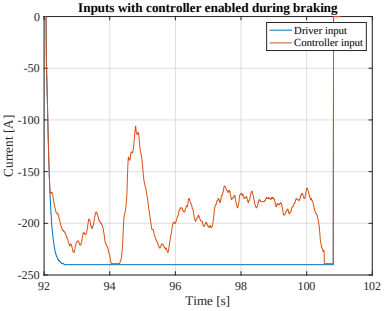

(f) Driver input during braking.

Figure B.3: Controller enabled during braking with an initial velocity of 30 km/h (left) and 50 km/h (right).

Bibliography

Amodeo, M., A. Ferrara, R. Terzaghi, and C. Vecchio (2010). "Wheel slip control via second-order sliding-mode generation". *IEEE Transactions on Intelligent Transportation Systems* **11**:1, pp. 122–131. DOI: 10.1109/TITS.2009.2035438.

Åström, K. J. and R. M. Murray (2020). *Feedback Systems*. Princeton University Press. Princeton, New Jersey. URL: https://fbswiki.org/wiki/index.php/Main_Page. (accessed: 11.07.2021).

Åström, K. J. and B. Wittenmark (2008). *Adaptive Control*. 2nd ed. Dover Publications. Mineola, New York.

Åström, K. J. and B. Wittenmark (2011). *Computer-Controlled Systems*. 3rd ed. Dover Publications. Mineola, New York.

Basrah, M. S., E. Siampis, E. Velenis, D. Cao, and S. Longo (2017). "Wheel slip control with torque blending using linear and nonlinear model predictive control". *Vehicle System Dynamics* **55**:11, pp. 1665–1685. DOI: 10.1080/00423114.2017.1318212.

Behrendt, M. (2009). *Wikimedia commons, m. b. via (2007). a basic working principle of model predictive control*. URL: https://commons.wikimedia.org/wiki/File:MPC_scheme_basic.svg. (accessed: 19.01.2021).

Bonci, A., R. D. Amicis, S. Longhi, and E. Lorenzoni (2018). "A smooth traction control design for two-wheeled electric vehicles". *2018 14th IEEE/ASME International Conference on Mechatronic and Embedded Systems and Applications (MESA). Oulu, Finland*, pp. 1–6. DOI: 10.1109/MESA.2018.8449199.

Bosch, G. R. (2011). *Bosch Automotive Handbook*. 8th ed. Wiley-Blackwell. The Atrium, Southern Gate, Chichester, West Sussex.

Chui, C. K. and G. Chen (2017). *Kalman Filtering*. 5th ed. Springer. Berlin.

Eriksson, L. and L. Nielsen (2014). *Modeling and Contol of Engines and Drivelines*. 1st ed. John Wiley & Sons. The Atrium, Southern Gate, Chichester, West Sussex.

Goodwin, G. C., S. F. Graebe, and M. E. Salgado (2000). *Control System Design*. 1st ed. Pearson Prentice Hall. Upper Saddle River, New Jersey.

Hamzah, N., M. K. Aripin, Y. M. Sam, H. Selamat, and R. Ghazali (2012). "Second order sliding mode controller for longitudinal wheel slip control". *IEEE 8th International Colloquium on Signal Processing and its Applications. Malacca, Malaysia*, pp. 138–143. DOI: 10.1109/CSPA.2012.6194706.

Hendricks, E., O. Jannerup, and P. H. Sørensen (2008). *Linear Systems Control*. 1st ed. Springer. Berlin, Heidelberg.

Johansen, A., I. Petersen, J. Kalkkuhl, and J. Ludemann (2003). "Gain-scheduled wheel slip control in automotive brake systems". *IEEE Transactions on Control Systems Technology. Capri, Italy* **11**:6, pp. 799–811. DOI: 10.1109/TCST.2003.815607.

Kalman, R. E. (1960). "A new approach to linear filtering and prediction problems". *Transactions of the ASME–Journal of Basic Engineering* **82**:Series D, pp. 35–45.

Kiencke, U. and L. Nielsen (2005). *Automotive Control Systems*. 2nd ed. Springer. Berlin Heidelberg, New York.

Liang, B.-R. and W.-S. Lin (2010). "Optimal regenerative torque control to maximize energy recapture of electric vehicles". *19-23 September, 2010 World Automation Congress. Kobe, Japan*, pp. 1–6.

Liu, W., H. Qi, and X. Liu (2020). "Evaluation of regenerative braking based on single-pedal control for electric vehicles". *Front. Mech. Eng* **15**:1, pp. 166–179. DOI: https://doi.org/10.1007/s11465-019-0546-x.

Mathworks (2021). URL: https://www.mathworks.com/help/physmod/sdl/ref/tireroadinteractionmagicformula.html. (accessed: 07.03.2021).

Omotion (2021a). URL: https://omotion.se. (accessed: 02.07.2020).

Omotion (2021b). *Omotion 2*. URL: https://omotion.se/omotion-2-technical-specification/. (accessed: 15.05.2021).

Rajamani, R. (2012). *Vehicle Dynamics and Control*. 2nd ed. Springer. New York, Dordrecht, Heidelberg, London.

Rawlings, J. B., D. Q. Mayne, and M. M. Diehl (2019). *Model Predictive Control: Theory, Computation and Design*. 2nd ed. CA Nob Hill Publishing, LLC Cheryl M. Rawlings.

Savaresi, S. M. and M. Tanelli (2010). *Active Braking Control Systems Design for Vehicles*. 1st ed. Springer. London.

Tanelli, M., C. Vecchio, M. Corno, A. Ferrara, and S. M. Savaresi (2009). "Traction control for ride-by-wire sport motorcycles: a second-order sliding mode approach". *IEEE Transactions on Industrial Electronics* **56**:9, pp. 3347–3356. DOI: 10.1109/TIE.2009.2018430.

Vasiljevic, G., K. Griparic, and S. Bogdan (2012). "Slip-based traction control system with an on-line road condition estimation for electric vehicles". *3-5 October, 2012 IEEE International Conference on Control Applications. Dubrovnik, Croatia*, pp. 395–400. DOI: 10.1109/CCA.2012.6402685.

Yuan, L., H. Chen, B. Ren, and H. Zhao (2015). "Model predictive slip control for electric vehicle with four in-wheel motors". *28-30 July, 2015 34th Chinese Control Conference (CCC). Hangzhou, China*, pp. 7895–7900. DOI: 10.1109/ChiCC.2015.726089.

Zhakatayev, A., B. Rakhim, O. Adiyatov, A. Baimyshev, and H. A. Varol (2017). "Successive linearization based model predictive control of variable stiffness actuated robots". *3-7 July, 2017 IEEE International Conference on Advanced Intelligent Mechatronics (AIM). Munich, Germany*, pp. 1774–1779. DOI: 10.1109/AIM.2017.8014275.

Lund University
Department of Automatic Control
Box 118
SE-221 00 Lund Sweden

Document name
MASTER'S THESIS

Date of issue
May 2021

Document Number
TFRT-6128

Author(s)
Andreas Karlin

Supervisor
Ola Svensson, Omotion AB, Sweden
Björn Olofsson, Dept. of Automatic Control, Lund University, Sweden
Anders Robertsson, Dept. of Automatic Control, Lund University, Sweden
Rolf Johansson, Dept. of Automatic Control, Lund University, Sweden (examiner)

Title and subtitle
Slip Control for a Three-Wheeled Electric Motorcycle

Abstract

The aim of this Master Thesis was to design, implement and test a slip controller for an electric three-wheeled motorcycle in order to prevent undesirable slip on the driving wheel during acceleration and regenerative braking. A PI controller was implemented for the two different cases and was tested through various experiments and driving conditions. Three different control strategies were also designed and compared through simulations, a PI, LQR and a MPC controller for both acceleration and braking were designed and tested through five different driving conditions. All three controllers show promising results to control the slip and the implemented PI controller was also able increase safety on slippery surfaces.

Keywords

Classification system and/or index terms (if any)

Supplementary bibliographical information

ISSN and key title
0280-5316

ISBN

Language
English

Number of pages
1-93

Recipient's notes

Security classification

http://www.control.lth.se/publications/